MASTER'S THESIS

ULTRAFAST ATOMIC FORCE MICROSCOPY

RASA REJALI

Department of Physics
McGill University
Supervision of DR. PETER GRÜTTER
July 2018

A thesis submitted to McGill University in partial fulfillment of the requirements of the degree of
Master of Science

Acknowledgements

First and foremost, I would like to thank my supervisor, Peter Grütter, for his kindness, guidance, and above all, his unwavering faith in his students; and additionally, for giving me the opportunity to work on this exciting, rewarding project. Thank you for everything!

I would like to thank all of the Grütter group members for eating pizza with me every Wednesday, and for providing support, insight, and laughter whenever necessary.

My days in the lab were brightened by my basement buddies: Zeno, Andreas, and Tyler! In particular, I would like to acknowledge the countless hours Zeno has devoted to teaching me experimental physics, and for being the best mentor anyone could ask for. He has taught me everything, from the inner workings of ultrahigh vacuum, to data processing in MatLab; and he has been there to save the day whenever I've failed—none of this would have been possible without Zeno! And, of course, a special thank you to Andreas and Tyler, for always having my back, helping me with all things vacuum, and lending a listening ear.

Thank you to Yoichi Miyahara, the heart and soul of the Grütter group! Your expertise in the various disciplines of physics leaves me amazed everyday; but your willingness to help and kind demeanor are even more wonderful.

Thank you to David Cooke, for teaching me everything I know about experimental optics, and for helping me whenever I needed it, without fail. The time you've invested is deeply appreciated.

I want to thank my best friend, Kays Haddad, for checking my math, making me dinner, and being pretty wonderful in general. And lastly, a massive thank you to my family, Sarvin, Saman, and Mohsen, for reminding me that a willingness to try hard and be happy are all that I need!

Contribution of Co-Authors

The following section is based on a manuscript prepared with co-authors, the contributions of whom are summarized as follows:

Sections 1 and 5 are based on *Nanoscale force sensing with attosecond precision* by Zeno Schumacher, Rasa Rejali, Raphael Pachlatko, Andreas Spielhofer, Yoichi Miyahara, David G. Cooke, and Peter Grütter. Z.S. and R.R. performed the experiment, Z.S. and R.R analyzed the data, Z.S., R.R., R.P., A.S. and Y.M maintained and improved the experimental setup. Z.S., D.C. and P.G. conceived the experiment, P.G. supervised the experiment. Z.S. and R.R. wrote the manuscript. All authors discussed the results and edited the manuscript.

Abstract

RASA REJALI

Ultrafast Atomic Force Microscopy

Developing a technique that combines nanometer spatial resolution with sub-femtosecond temporal resolution is a crucial step towards exposing the inner mechanisms of chemical reactions, single molecule motion, electron dynamics in solids, and the effects of defects or trap states on electron motion and behavior, amongst a slew of other questions related to the ultrafast electron dynamics of surfaces.

In this work, we integrate a traditional pump-probe spectroscopy scheme into an ultra-high vacuum atomic force microscope to develop the first ultrafast atomic force microscope capable of measuring nanoscale forces with attosecond precision. We use this technique to measure and spatially resolve local changes in electric polarization in a common, and well characterized, nonlinear material: lithium niobate. In particular, we exploit the strong second-order nonlinear susceptibility of lithium niobate to produce an electric polarization proportional to the incoming electric field of two $\sim$100 fs, 780 nm laser pulses. The induced polarization change in lithium niobate generates an electrostatic force that is detected, and spatially resolved, using non-contact AFM.

Furthermore, we use our technique to experimentally verify that the fundamental sensitivity limit of force detection in non-contact AFM, which is determined by the thermal noise, also dictates the minimal temporal resolution that can be achieved. We present a generalization of our time-resolved AFM technique for measuring any light-matter interaction that results in a measurable force.

Résumé

RASA REJALI

Microscopie Ultrarapide à Force Atomique

La développement d'une technique combinant la résolution spatiale nanométrique et la résolution temporelle sous-femtoseconde est une étape cruciale pour exposer les mécanismes internes des réactions chimiques, les mouvements moléculaires, la dynamique des électrons dans les solides et les effets des défauts ou états des pièges sur le mouvement et le comportement des électrons, parmi une foule d'autres questions liées à la dynamique ultrarapide des électrons des surfaces.

Dans ce travail, nous intégrons un schéma de spectroscopie pompe-sonde traditionnel dans un microscope ultra-vide à force atomique pour développer le premier microscope à force atomique ultrarapide capable de mesurer les forces nanométriques avec une précision d'attoseconde. Nous utilisons cette technique pour mesurer et résoudre spatialement les changements locaux de la polarisation électrique dans un matériau commun non linéaire et bien caractérisé: le niobate de lithium. En particulier, nous exploitons la forte susceptibilité non linéaire de deuxième ordre du niobate de lithium pour produire une polarisation électrique proportionnelle au champ avec période $\sim$100 fs et longeur d'onde 780 nm électrique entrant de deux impulsions laser. Le changement de polarisation qui est induit dans le niobate de lithium génère une force électrostatique qui est détectée et résolue spatialement, en utilisant AFM sans contact.

En outre, nous utilisons notre technique pour vérifier expérimentalement que la limite de sensibilité fondamentale de la détection de force dans l'AFM sans contact, qui est déterminée par le bruit thermique, dicte également la résolution temporelle minimale qui peut être obtenue. Nous présentons une généralisation de notre technique d'AFM résolue en temps pour mesurer n'importe quelle interaction lumière-matière qui résulte en une force mesurable.

Contents

Dedicated to Sarvin & Mohsen,
my loving parents.

Chapter 1

Introduction

Since their invention in the mid 1980s, scanning probe techniques, like atomic force microscopy (AFM) and scanning tunneling microscopy (STM), have become typically favored methods of surpassing the diffraction limit of optical techniques to obtain real-space, atomically resolved images of surfaces. A continued theme in scanning probe research has been to develop tools and techniques for reliably characterizing structure-function relationships on the nanoscale. Along these lines, one of the most significant challenges facing the community was to develop a variant of the scanning probe microscope, which would combine the sub-nanometer resolution characteristic of AFM or STM with optical spectroscopic capabilities that would allow for the time resolution necessary to study nanoscale ultrafast dynamics. Thus, it follows that new methods for probing and controlling nanoscale physics on ultrafast time scales are continually under development, with progress in the field being largely spearheaded by instrumentation development [1–3].

In its most common realization, AFM is an inherently slow technique: for example, the resonant frequency of a typical cantilever in vacuum is between 0.1–1 MHz, and the time constant of the feedback electronics is usually in the range of milliseconds [4, 5]. For much of its tenure as a surface science characterization tool, this has led to the assumption that phenomena occurring faster than the cantilever resonance cannot be resolved using AFM [6, 7]. However, slow detection does not have to render a detector useless for ultrafast measurements: indeed, most photodetectors used for optical ultrafast measurements are much slower than the physics they probe. In fact, the most recent advances in ultrafast photodetectors have resulted in response times on the order of a few picoseconds—still much slower than the timescales associated with most ultrafast phenomena [8, 9].

The first study to propose a general technique for achieving ultrafast time resolution in scanning probe microscopies was presented by R. Hamers and D. G. Cahill

in 1990 [10]. The authors demonstrated that time resolution faster than the bandwidth of the detection electronics was possible: by using a pulsed illumination scheme, they were able to exploit the inherent nonlinearities of photocarrier dynamics to achieve nanosecond temporal resolution with scanning capacitance microscopy [10, 11]. This general technique has been implemented by various research groups since, to measure minority carrier lifetimes, recombination rates in photovoltaics, photodynamics in semiconductors, and time-resolved changes in surface photovoltage—all in the micro- to millisecond range [12–15]. Only recently has the time resolution of AFM advanced beyond the resonance frequency of the mechanical oscillator, with picosecond resolution—the fastest to date—reported by Schumacher *et al.* on low-temperature grown GaAs [16].

Conversely, adapting ultrafast measurement techniques to STM has generally followed a faster trajectory, and several research groups have succeeded in demonstrating picosecond time resolution by means of optical pump-probe excitation and non-linear mixing in the tunnel junction [17–24]. Most recently, sub-50 fs temporal resolution has been demonstrated by using the light field of a phase-stable THz pulse to gate the tunnel current of a STM measurement [21, 25–27]. These landmark achievements have significantly impacted the scanning probe community, making heretofore impossible experiments a reality. However, the shortcomings of an ultrafast STM must also be noted: first, samples are restricted to conductive species; and second, thermal expansion caused by incident laser light can produce small perturbation of the tunnel gap, and therefore lead to measurement artifacts [16].

These are limitations that would be rectified by the development of an ultrafast AFM. Thus, the cumulative efforts expended by researchers over the past few decades to achieve time resolution in AFM are well-justified, as are the continued attempts to improve this time-resolution. AFM is uniquely able to spatially resolve molecular structure, surface potential [28], as well as local density of states [29–31]. In this work, we present a general technique for achieving attosecond temporal precision with an ultra-high vacuum (UHV) AFM.

Chapter 2

Nanoscale Force Detection

The invention of the scanning tunneling microscope (STM) by Binnig and Rohrer in 1982 gave new meaning to research in nanotechnology: since the first atomically resolved images of the Si(111)7×7 surface were acquired, the capabilities of scanning probe techniques for nanoscale characterization and real space imaging of atomic structure quickly became evident—and indispensible—to the surface science community [32]. Only four years later, the major limitation of STM—the need for conducting surfaces—was shortly rectified by the development of the atomic force microscope (AFM), which expanded the range of measurable samples to include non-conductive species, such as insulators and dielectric [33].

The basic working principle of AFM was initially based on scanning a tip, supported by a cantilever beam, across a surface in contact, while continuously recording the deflection of the beam to extract surface topography. Further progress led to the development of another mode of AFM: non-contact (or dynamical) AFM (nc-AFM) [34]. In this mode, the cantilever is vibrated near its resonance frequency, and changes in the vibration arising from tip-sample interactions are measured.

Several factors have contributed to making nc-AFM the powerful, versatile, and frequently-used technique it has become today: first, it regularly allows for nanometer spatial resolution; second, the probe can be used for topographical imaging and general characterization of the surface; and lastly, it records several parameters that are sensitive to tip-sample interactions (phase shift, amplitude, frequency shift, so forth) [35]. The combination of AFM with other experimental methods has led to the development of a wide range of research fields, which have aimed at accessing additional sample properties on the nanoscale.

The two major operating modes of nc-AFM are amplitude-modulated (AM) [34, 36] and frequency modulated [5]. In AM-AFM (tapping mode), the cantilever is

driven near or at its free resonance frequency. In this case, the feedback parameter used to extract topography is the cantilever oscillation amplitude. Additionally, the phase shift between the excitation and the tip oscillation traces changes in the sample properties. In FM-AFM (non-contact mode), the cantilever is driven at its resonance frequency with a fixed oscillation amplitude. However, this resonance frequency is a function of the forces acting between tip and sample: the source of contrast thus arises by tracking the difference in the free resonance and the measured resonance as the tip is scanned over the surface. An important practical distinction between these operation modes is that AM-AFM is well suited to measurements performed in air or liquid, while FM-AFM is optimal for use in UHV. This distinction arises because the quality factor of the cantilever is higher in vacuum $(Q \sim 10^4)$, and this results in very slow feedback responses for AM-AFM; in contrast, the additional feedback loop needed for FM mode would make it too slow and unnecessarily complicated for operation in air or liquid [35]. This chapter will describe the working principles of FM-AFM, the dominant mode used for measurements presented in this thesis.

2.1 Principles of Frequency Modulated AFM

FM mode was developed by Albrecht *et al.* as a way to achieve heightened measurement sensitivity by means of an increased Q-factor, while ensuring no restrictions on the bandwidth [5]. In both operational modes of nc-AFM, the equation of motion (EOM) of the cantilever-tip ensemble under the influence of tip-sample interaction forces must be solved.

Though a rigorous approach must consider the 3D equation of motion [37–39], most consider the cantilever-tip system as a point-mass spring, which reduces the equation of motion for the direction perpendicular to the surface $z(t)$ (Figure 2.1) to a nonlinear second-order ODE:

$$m\ddot{z}(t) + \frac{mQ}{\omega_0}\dot{z}(t) + kz(t) - F_{ts}[z_c + z(t)] = F_{exc}(t) \tag{2.1}$$

where F_{exc} denotes amplitude of the driving force, m the mass, and z_c the average tip-sample separation; Q, $\omega_0 = 2\pi f_0$, and k denote the quality factor, the angular resonance frequency, and the force constant of the free cantilever, respectively; and F_{ts} the tip-sample interaction force. In the absence of tip-sample forces, equation 2.1 reduces to describe a driven damped harmonic oscillator.

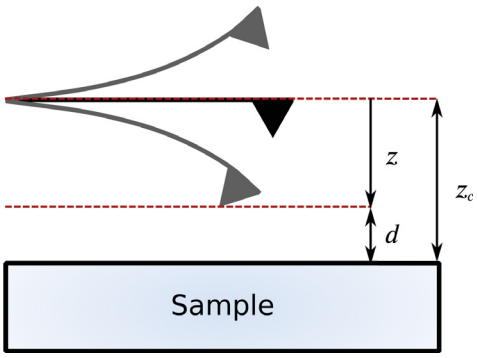

FIGURE 2.1: Schematic of the cantilever-tip ensemble, demonstrating the spatial distances in dynamic modes of AFM. The average separation between the tip and sample surface is given by z_c; the instantaneous position of the tip, given by z, is defined relative to this rest position. The tip-sample separation d is the difference between z_c and z. Figure adapted from [35].

In general, trying to relate the measured experimental frequency shift to the tip-sample force is a complex problem, partly because F_{ts} is inherently anharmonic. Furthermore, $F_{exc}(t)$ is not perfectly harmonic either: the amplitude and frequency of the excitation are not constants, but rather dependent on the control electronics where the signal originates. Specifically, an amplifier receives the beam-deflection detection signal and adjusts the amplitude the excitation signal to keep the oscillation amplitude of the cantilever constant. Additionally, it shifts the phase of the excitation to resonantly excite the cantilever. Thus, this feedback loop (schematically depicted in figure 2.2) ensures the cantilever maintains constant amplitude and is being driven at its current resonance frequency. To account for this, Gotsmann *et al.* proposed a model for describing the excitation force for a PI controller [40]:

$$F_{exc}(t) = R(t)z(t - t_{phase}). \tag{2.2}$$

A time delay, t_{phase}, is used to verify the driving force is resonant with the cantilever oscillations. $R(t)$ denotes the loop-gain function, and is contingent on the current and previous values of the cantilever oscillation amplitude $A(t)$, the targeted amplitude A_0, and the PI controller settings, such as the proportional gain p and the integral gain i:

$$R(t) = p[A(t) - A_0] + i \int_{t'=0}^{t} [A(t') - A_0]\, dt \tag{2.3}$$

By property of maintaining a constant vibration amplitude, the feedback loop ensures that energy loses, whether they arise from the cantilever or from tip-sample forces, are completely nullified by the excitation signal. Therefore, the driving (F_{exc}) and damping terms ($\propto \dot{z}(t)$) in equation 2.1 can be discarded, yielding [41]:

$$m\ddot{z}(t) + kz(t) - F_{ts}[z_c + z(t)] = 0 \tag{2.4}$$

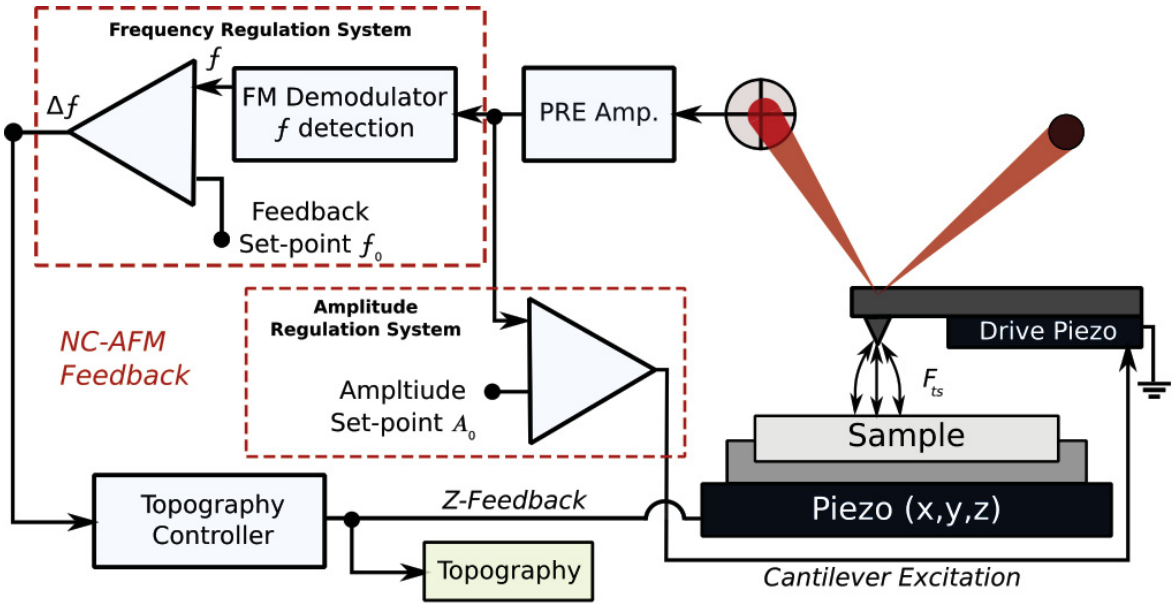

FIGURE 2.2: Experimental configuration of FM-AFM. A laser diode and four-quadrant photodiode are used to track the motion of the cantilever. The beam-deflection signal is fed to both the amplitude regulation system and the FM demodulator. The amplitude control maintains the oscillation amplitude of the cantilever at a constant set value, A_0. By comparing the current amplitude to the set-point, this regulation system applies the correct excitation signal to the cantilever drive piezo. Similarly, the FM demodulator extracts the frequency shift of the cantilever by comparing the current resonance, f, to the set point f_0. The frequency shift is then sent to the topography controller, which controls the z-position of the sample piezo to maintain a constant Δf and extract a topographical image.

Additionally, the assumption that the interaction force F_{ts} can be linearized around z_c is valid in the small oscillation amplitude limit. In that case,

$$m\ddot{z} + (k + k_{ts})z(t) = 0 \quad \text{with} \quad k_{ts}(z_c) = -\left.\frac{\partial F_{ts}}{\partial s}\right|_{s=z_c} \tag{2.5}$$

In the limit that $k_{ts} \ll k$, it is possible to Taylor expand around $k_{ts}/k = 0$ to arrive at an analytical expression for the frequency shift in terms of the force gradient:

$$\Delta f(z_c) = \frac{f_0}{2k} k_{ts}(z_c) = -\left.\frac{f_0}{2k}\frac{\partial F_{ts}}{\partial s}\right|_{s=z_c} \tag{2.6}$$

However, if the oscillation amplitude is large with respect to the tip-sample interaction range, then the above-stated approximation is not valid. For common oscillation amplitudes ($\sim$100Å) and stiff cantilevers ($k \sim 20 - 30$N/m), the potential energy of the cantilever ($kA_0^2/2$) is large compared to the energy of typical tip-sample

interactions (1-10 eV) [35]. In this case, the tip-sample system can be described as a weakly perturbed harmonic oscillator. Thereby, the frequency shift can be derived using first order perturbation theory, as initially shown by Giessibl [41]. Several different perturbation schemes for large-amplitude oscillation have followed since [42–48], but the common central result establishes a relationship between the frequency shift and the average tip-sample force during a full oscillation cycle:

$$\Delta f(d, k, A_0, f_0) = -\frac{f_0}{kA_0^2}\langle F_{ts} z\rangle \tag{2.7}$$

$$= -\frac{1}{2\pi}\frac{f_0}{kA_0}\int_0^{2\pi} F_{ts}[d + A_0 + A_0\cos(2\pi f_0 t)]A_0\cos(2\pi f_0 t)\, dt \tag{2.8}$$

Unlike the small-amplitude result (equation 2.6), the large-amplitude expression above depends on the distance of closes approach, d, as well as the operational oscillation amplitude.

Having understood the relationship between measured frequency shift Δf and tip-sample forces F_{ts} it is useful to investigate the origin of these interactions and the different types of tip-sample forces that are relevant to, and dominate, AFM measurements.

2.2 Interaction Forces

Tip-sample interactions are comprised of various short- and long-range forces—but those relevant to AFM are in almost all cases electromagnetic in origin. The intermolecular, surface, and macroscopic sample features resulting in tip-sample interactions are encompassed by the following: van der Waals forces, short-range repulsive and chemical binding forces, electromagnetic forces, and long-range electrostatic forces.

The empirical Lennard-Jones potential, shown in figure 2.3, is used to describe short-range interactions [50]. At small tip-sample separation distances, the Lennard-Jones short-range force is repulsive. As the tip-sample distance is increased, the interaction force becomes attractive, reaches a global minimum, and then asymptotically approaches zero. For dipole-dipole interactions, this is quantitatively delineated by the Lennard-Jones potential at a distance r [50]:

$$U_{LJ} = -4\epsilon\left[\left(\frac{\sigma_0}{r}\right)^6 - \left(\frac{\sigma_0}{r}\right)^{12}\right], \tag{2.9}$$

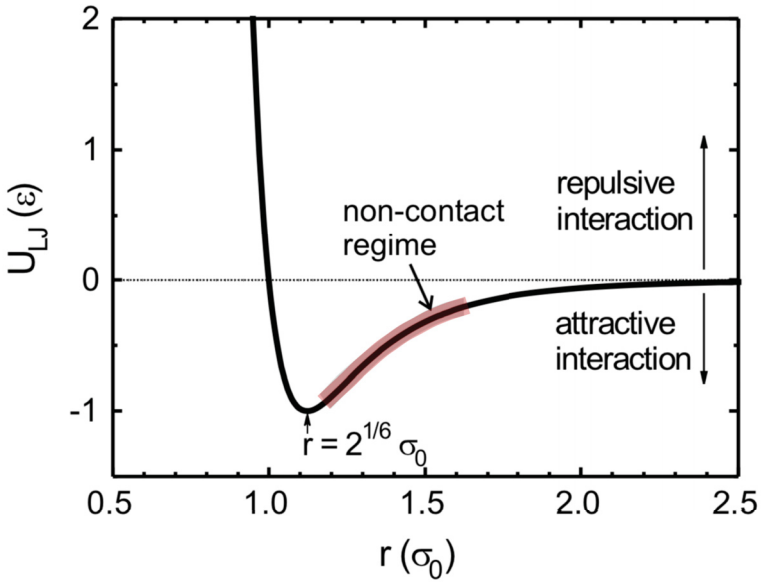

FIGURE 2.3: The Lennard-Jones potential. This potential is usually used to described short-range tip-sample interactions. Nc-AFM operating conditions typically lie in the attractive region of this interaction. Figure from [49].

where σ_0 is the characteristic length and ϵ an empirical constant that denotes the characteristic tip-sample interaction energy.

For very small tip-samples distance, the electron clouds of the tip and sample atoms overlap, resulting in repulsive forces due to the Pauli exclusion principle. At distances below $\sim$ 5Å, a bonding state of the quantum mechanical overlap between the tip and sample wavefunctions exists—this gives rise to chemical forces with an exponential distance dependence [51].

The van der Waals force F_{vdW} arises from interactions of induced dipoles between atoms and molecules and constitutes a constant contribution to the attractive region of the short-range force. To analytically describe the van der Waals force in AFM, the sample surface is modeled as an infinite plane and the tip as a sphere of radius R [35, 50]:

$$F_{vdW} = -\frac{HR}{6d^2}, \tag{2.10}$$

where H denotes the Hamaker constant and d the closest tip-sample separation distance. If the tip-sample distance is smaller than intermolecular distances, the adhesion force substitutes the van der Waals force.

The final dominant contribution to tip-sample interactions is the electrostatic force. In the AFM perspective, the tip-sample system can be modeled using a parallel-plate capacitor with energy $U_{el} = 1/2CV^2$, where C denotes capacitance and V the voltage applied between tip and sample. Thus, in the absence of free charges the

electrostatic force is:

$$F_{el} = - \bigtriangledown U_{el} = \frac{1}{2}\frac{\partial C}{\partial z}V^2 + CV\frac{\partial V}{\partial r}, \tag{2.11}$$

However, the AFM is sensitive to forces acting perpendicular to the sample surface, and thus the spatial gradient reduced to a 1-dimensional derivative:

$$F_{el} = -\frac{1}{2}\frac{\partial C}{\partial z}V^2, \tag{2.12}$$

It is worth noting that the electrostatic force is always attractive, because $\partial C/\partial z < 0$.

The above-mentioned short- and long-range forces all contribute to the tip-sample interactions measured in AFM. Depending on experimental conditions, such as the tip-sample distance and the sample properties, it is often possible to determine the dominant force acting on the tip and use this information to relate the measured frequency shift to a real force. However, as equation 2.8 indicates, the measured frequency shift is proportional to the *time average* of the force over a full oscillation cycle of the tip—and this may lead to the assumption that forces happening faster than the period of this oscillation cannot be resolved. By exploiting the inherent nonlinearities of the sample response, it is possible to overcome this apparent limitation. In the following, the true lower limit of time resolution in FM mode AFM, as originally demonstrated by Schumacher *et al.* will be explained [16].

2.3 Lower Limit of Time Resolution in FM-AFM

To determine the minimum achievable time resolution in FM-AFM for a general external stimulus and a *nonlinear* sample response, it is useful to view the problem from the perspective of energy changes rather than forces, as originally proposed by Hamers and Cahill [10].

Consider the potential energy of the AFM cantilever, $U(t)$, subject to some time-dependent tip-sample interaction, $U_{ts}(t)$, resulting from the external stimulus, $S(t)$; assume this interaction results in some detectable change in the measured frequency shift [16, 35, 41, 42, 52]. The applied stimulus can take any form— optical, thermal, magnetic, electric—as long as the modulation it induces causes a measurable change.

For the sake of simplicity, we will consider that $S(t)$ is a pulse train, as depicted in figure 2.4. For the duration of the pulse, T_p, the tip-sample interaction energy change

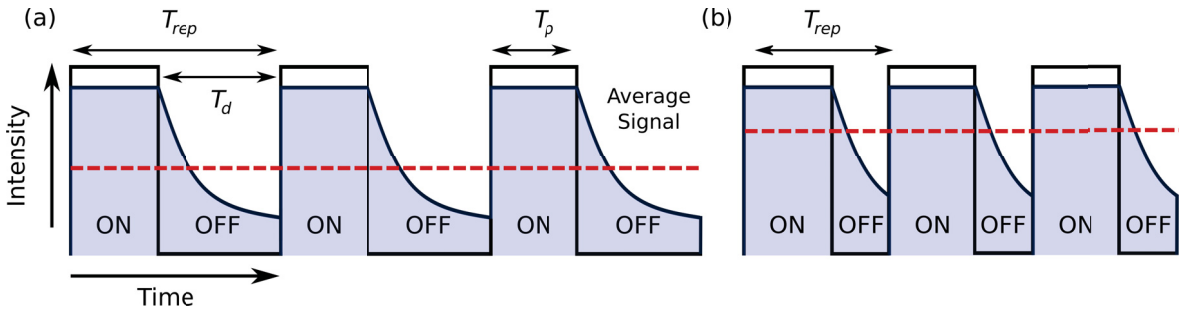

FIGURE 2.4: The external modulating signal, $S(t)$ (solid black line) plotted against time for (a) long and (b) short delay times, T_d. The corresponding change in the tip-sample interaction energy (blue) is also shown. As indicated, the average signal changes as a function of the delay time. Figure adapted from [53]

can be approximated to be a constant U_0. The rise time of the sample response must be much shorter than the pulse duration for this approximation to hold. Once the external stimulation turns off, the sample response decays according to a characteristic response time τ:

$$\Delta U(S(t)) = \begin{cases} U_0 & \text{for} \quad 0 < t < T_p \\ U_0 e^{-(t-T_p)/\tau} & \text{for} \quad T_p < T < T_{rep} \end{cases} \tag{2.13}$$

The aim of using an AFM to measure this modulation in the tip-sample interaction is to extract the decay time τ. If τ is much shorter than the oscillation period of the cantilever (1-10 μs) and the detection electronics, then the AFM does not have the ability to resolve a single cycle of this light-on, light-off modulation. Instead, the cantilever measures over many cycles of the modulation, and therefore detects the average response of the system.

In fact, the measured average signal will depend on the delay time between two consecutive pulses, as well as the decay time of the system response. Thus, by varying T_d many times over and recording the average signal each time, it is possible to reconstruct the original event and extract decay times much faster than the oscillation period of the cantilever.

The only requirement is that the energy difference between two different delay times is measurable. Thus, the cantilever oscillation and slow feedback electronics are no longer relevant; instead, the minimal detectable energy by FM-AFM is the limiting factor. To determine this lower limit, it is necessary to define the average potential energy over one cycle of the pulsed stimulation, T_{rep}:

$$\langle \Delta U(S(t)) \rangle = \frac{\tau U_0}{T_{rep}} \left(1 - e^{-T_d/\tau} - e^{-(T_{rep}-T_d-2T_p)/\tau} \right) \tag{2.14}$$

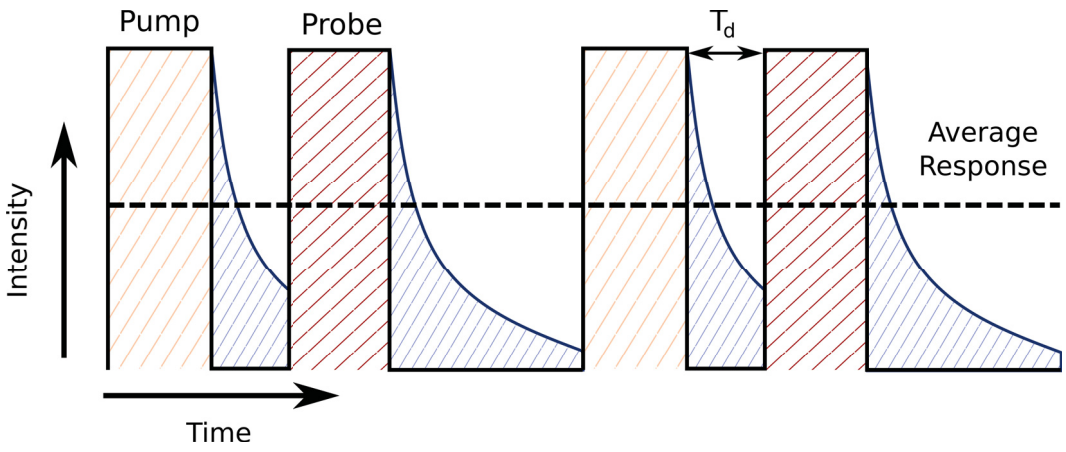

FIGURE 2.5: Two pulse trains modulating the tip-sample interaction are shown: the pump (yellow shading) and probe (red shading). The time delay (T_d) between the pump and the probe is defined. The average potential energy change caused by the external stimulus is also shown. For simplicity, we assume the pump and probe pulses incite the same response amplitude. Physically this corresponds to the case in which the both pump and probe pulses excite all the carriers in the probe volume, thereby saturating the response signal. Figure adapted from [53].

If $T_{rep} \gg T_p, T_d$, and τ, then $e^{-(T_{rep}-T_d-2T_p)/\tau} \rightarrow 0$, thus yielding an easy relationship between average energy changes and decay time. For FM-AFM, the minimum energy change detectable for on-resonant operating conditions is determined by the thermal noise [5]. As shown by Schumacher *et al.*, by equating the average energy change (equation 2.14) to the thermal noise limit it is possible to extract the lower limit of time resolution in AFM:

$$\tau = \frac{T_{rep}}{U_0(1-e^{-\beta})}\frac{2k_BT}{\pi f_0 Q \tau_s}, \tag{2.15}$$

where β is T_d/τ, and τ_s is the experimental integration time [16]. Though it is not possible to analytically isolate τ in equation 2.15, the dependence of τ on k_BT is still demonstrated. This results holds if instead of a single pulse train, there are two pulse trains (pump and probe) that can be delayed in time with respect to each other, as shown in figure 2.5. This has been implemented experimentally using FM-AFM and a pump-probe scheme to measure picosecond photocarrier decay in low-temperature grown GaAs with a cantilever frequency of 280 kHz [16].

The fundamental result that the lower limit of time resolution in FM-AFM is governed by thermal noise serves as the basis for ultrafast AFM measurements. This principle is implemented in this thesis for the development of an AFM capable of femtosecond temporal resolution, the instrumentation details of which follow in the next chapter.

Chapter 3

Experimental Techniques & Methods

The development of an ultrafast FM-AFM is contingent on two fundamental techniques: UHV-AFM, and ultrafast optical methods. The technical realization of an ultrafast AFM is quite challenging and intricate, partly because it is a multi-fold problem: the optical and AFM instrumentation must first be independently functional, and then successfully integrated. This process hinges on coupling the excitation into the UHV, and directing it precisely at the tip-sample junction.

Thus, it is necessary to understand the experimental configuration of the UHV-AFM used to perform measurements, as well as the ultrafast laser system used to modulate the tip-sample interaction. To this end, technical details, such as the optical set-up, the laser integration, as well as potential challenges and pitfalls, are detailed below.

3.1 Ultra-High Vacuum AFM

A commercial JEOL JSPM 4500A UHV AFM (Figure 3.1) is used to perform all the measurements presented in this thesis. This UHV system is comprised of three chambers: a treatment chamber, equipped with tools for sample synthesis and preparation; a main chamber, in which an AFM and SEM are located—and can be used simultaneously—for sample characterization; and finally, an exchange chamber used for transferring samples or cantilevers between air and UHV.

The main and preparation chambers are each equipped with a diode type sputter-ion pump (300 L/s for N_2, and 90 L/s for Ar, Satsuki SIP-300XH-T16) and titanium sublimation pump (1,600 L/s for N_2, ULVAC PGT-3F), which work together to form a very efficient pumping system. Accordingly, the base pressure in the preparation

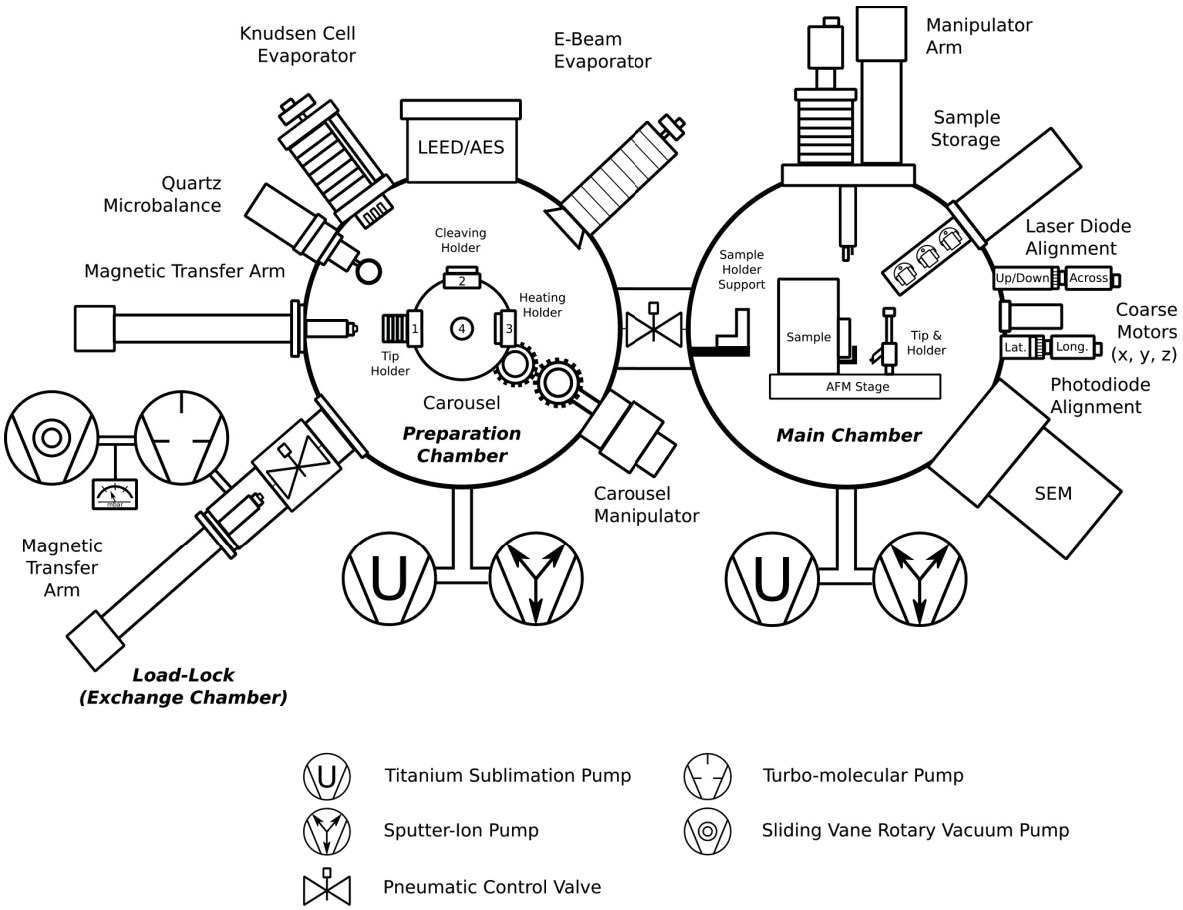

FIGURE 3.1: Schematic of the JEOL JSPM 4500A UHV AFM, depicting the three chambers (exchange, preparation, and main), the pumping system, and the surface science preparation and measurement tools available.

chamber is routinely in the 10^{-11} mbar range, and slightly higher at 10^{-10} mbar in the main chamber. A small leak from the SEM is responsible for the pressure discrepancy between the two chambers.

The load-lock is pumped by a turbo-molecular pump (TMP) (210 L/s for N_2, Pfeiffer TMU 261) and backed by a sliding vane rotary vacuum pump (9.7 m3/hr, Adixen 2010SD). Two magnetically coupled transfer arms allow for transfers inside vacuum: the first between the exchange and preparation chamber, and the second between the preparation and main chamber.

To accommodate tips and samples, a carousel is located inside the preparation chamber that allows for the storage of a maximum of four tip- or sample-holders. Positions 1–3 (figure 3.1) are additionally equipped with electrical contact to allow for sample annealing. Additionally, the carousel can be manipulated to allow samples access to the various preparation tools available within vacuum. Sputtering, molecular evaporation, LEED, electron beam metal evaporation, and crystal cleaving can be performed in situ, though those capabilities are not taken advantage of

in this work.

The measurement chamber houses the most important part of the entire system: the AFM. Once samples or tips are transfered to the main chamber, a so-called elevator arm is used to transfer them to the AFM stage. The elevator arm extracts and deposits samples/tips by using an electromagnetically actuated pin that couples to a hole on the top of the holders.

The sample is placed on a piezo tube that can extend 5μm in the x- and y-directions and 1.4μm in the z-direction. This functionality is used for scanning and fine positioning within the piezo range. The coarse positioning is controlled by gears and levers arms inside the UHV that are magnetically synced by rotary feedthroughs to external motors.

The resonance frequency of the cantilever is tracked using a conventional optical beam deflection system: a laser beam is focused on the cantilever and the reflected beam is detected using a photodiode. In particular, a 670 nm laser diode (Hitachi HL6714G) is operated at a constant current using a low noise controller (Thorlabs LDC 201C). A radio frequency modulator is used to modulate the DC laser bias, which reduces the coherence length of the beam and thereby increases stability by reducing interference. The beam reflected off the cantilever hits a mirror, and is consequently directed to the 4-quadrant photodiode. The lateral position of the mirror and longitudinal position of the photodiode can be controlled to get the beam centered on the 4-quadrants. Notably, a bandpass filter centered at 670nm with a 30nm bandwidth (Chroma Technology Corp, NC611498, ET670/30nm) is placed in front of the photodiode to filter stray light from the ultrafast laser used for sample excitation. Of course, the bandpass filter acts to filter out any other stray light during normal operation as well.

3.2 Technical Realization of an Ultrafast AFM

To perform time-resolved measurements with AFM, it is necessary to integrate an ultrafast laser system into the existing vacuum system, and to reliably couple the light to the tip-sample junction with precision. The experimental obstacles to achieve this are numbered: first, the mechanical vibrations of the laser and UHV must be isolated; the excitation laser cannot interfere with the cantilever detection system; the position of the cantilever is subject to change, and so the laser position inside the UHV must be easily controllable externally; and finally, the geometric restrictions

imposed by the physical location of the UHV viewports and the AFM stage must be respected.

Additionally, the choice of excitation is critical. Parameters such as the wavelength, fluence, pulse duration, and repetition rate determine the type of experiments that can be performed, and on what samples. For example, the pulse duration of the laser determines the time resolution achievable. Also, the energy of the laser pulse must correspond to the energy scales associated with the sample and the phenomenon under study. For example, to study exciton generation and decay under resonant excitation conditions, the laser wavelength must correspond to the excitonic level of the sample in question. The fluence of the laser must also be accounted for: one must evaluate if the fluence of the excitation is sufficiently high to observe the phenomenon under question, or rather if it is too high and might cause bleaching or damage to the sample. Ultimately, it is important to understand the capabilities and limitations of the excitation source, and to account for them in one's choice of experiment.

Such considerations, along with the experimental challenges and possible solutions accompanying the integration of a laser source in UHV-AFM will be discussed in the following. The ultrafast laser system used in this work will be explained as well.

3.2.1 Ultrafast Laser System

Mode-locked femtosecond lasers are a common tool for performing ultrafast spectroscopy. Traditionally, Ti:Sapphire sources have been favored for scientific purposes due to their pulse characteristics, tunability, and power output, despite the technical day-to-day challenges they often present to the user. However, the space constraints imposed by the lab space and the sizable UHV AFM itself, a more compact and user-friendly option proved necessary for our specific application. Thus, our sources consist of two plug-and-play fiber-based ultrafast pulsed lasers: the Toptica FemtoFiber Pro near infrared (NIR) and tuneable visible (TVIS) lasers. The NIR laser is used exclusively in this thesis.

The NIR laser is a mode-locked Er:fiber system based on direct pumping from fiber-pigtailed laser diodes and fiber integrated telecommunication components [54]. Specifically, the active laser medium is comprised of a Er-doped core-pumped fiber. A schematic of the laser is shown in figure 3.2. A saturable absorber mirror (SAM) inside the ring cavity allows for easy, self-starting mode-locking. In other words,

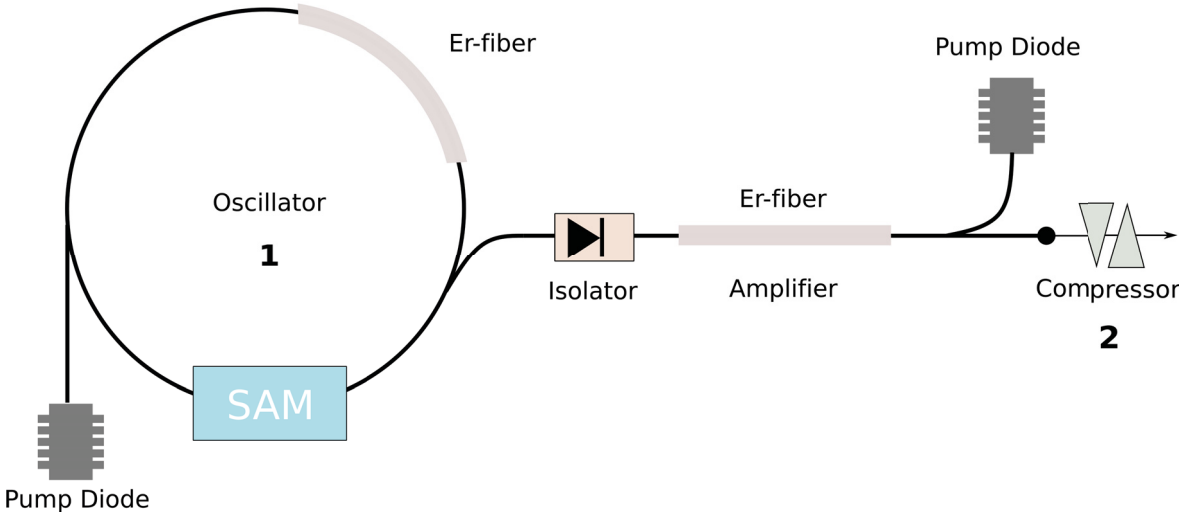

FIGURE 3.2: Schematic of the mode-locked Er-fiber laser system. The two fold process—first, the mode-locked ring oscillator to produce the beam, and second, the pulse compression—produces beams with $>$ 360 mW power, sub-100 fs pulse width, and 80 MHz repetition rate, centered at 1560 nm. Figure adapted from [54].

the SAM selects and amplifies pulses with a specific amplitude, and in doing so favors mode-locked operation over continuous-wave mode. The pulses generated by the mode-locked ring oscillator have a repetition rate of 80 MHz and center wavelength of 1560 nm. The duration of the pulses is controlled via a motorized Si prism compressor, that can be externally electronically optimized by the user.

The NIR laser can also produce a second beam at 780 nm through second-harmonic generation, though both wavelengths are not available concurrently. To switch between the fundamental (1560 nm) and the second harmonic (780 nm), a mechanical switch is used to either insert or remove a mirror from the beam path, as shown in figure 3.3. In the case of the former, the fundamental is reflected to the secondary aperture and emitted for use. In the case of the latter, the beam is allowed to propagate towards a second mirror which redirects the beam into a second-harmonic generation (SHG) unit.

The SHG unit is comprised of three parts: a focusing lens, nonlinear crystal, and collimating lens. The first lens focuses the beam into periodically poled lithium niobate (PPLN) for second-harmonic generation. The PPLN is housed inside a temperature controller that maintains the temperature of the crystal at $\sim 70^{\circ}$ for SHG phase-matching at 1560nm to be satisfied [55]. The emitted beam is then re-collimated and filtered so only the 780 nm beam continues to propagate. Before the beam exits the laser, a fraction of it is split to measure the power of the light, and this measurement is used to adjust the gain of the pulse generation. Due to inherent inefficiencies of the SHG process, the power of the second harmonic is substantially lower than the

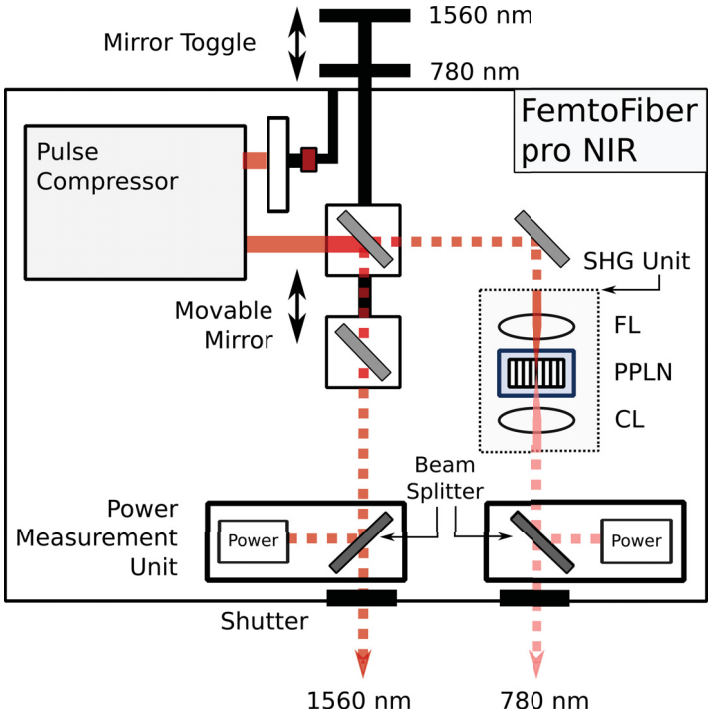

FIGURE 3.3: Following the generation of the 1560 nm pulses, the fiber is coupled to a collimator for beam propagation in free space. It first passes through the Si prism pulse compressor to produce < 100 fs pulses. If the desired output wavelength is 1560 nm, the beam is directly passed for emission. To output 780 nm, the beam is instead passed to a second-harmonic generation unit and then emitted.

fundamental at typical values > 140 mW. The 780 nm output is used for all measurements presented in this thesis.

3.2.2 Integration into an UHV Environment

To physically integrate the laser into the UHV system, it is necessary to ensure the integrity of the AFM is preserved and that the beam inside the UHV can be 1) controlled and 2) easily monitored.

To address these requirements, Z. Schumacher developed a stick-slip piezo-based movable mirror (figure 3.4) that sits inside the UHV and can be externally controlled to steer the beam with high precision [53]. The optics outside the UHV are used to direct the beam through a UHV viewport and onto the center of the movable mirror; the mirror is then finely positioned so that the beam is directed exactly at the tip sample junction. Two separate cameras are used to track the position of the beam inside the UHV: one focused on the movable mirror, and another on the sample surface.

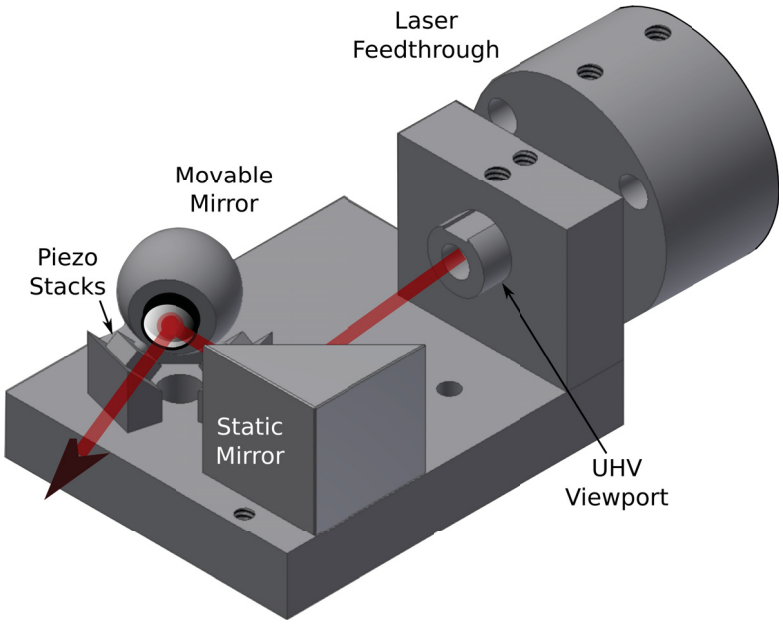

FIGURE 3.4: Schematic of the movable mirror assembly. The beam enters into UHV through the laser feed-through. It is then incident on a static mirror that redirects the beam onto the stick-slip piezo mounted mirror. The position of the mirror can be controlled externally by applying a high voltage sawtooth signal to the piezo stacks, giving the mirror free range of motion in both the lateral and longitudinal directions. Figure from [53].

The versatility alloted by this design means the optical set-up can accommodate any variations in tip or sample position, and that the beam inside the chamber can be easily visually tracked. This design also allows us to work around the geometric restrictions imposed by the AFM stage and UHV components, since we have complete control over the beam propagation inside the vacuum.

As mentioned previously, to ensure the excitation laser does not interfere with the beam-deflection system detailed in section 3.1, a narrow band-pass filter is used to filter any stray excitation light from the photodetector. This allows for routine operation of the AFM, despite the incorporation of the NIR laser source. Additionally, by using free-space propagation instead of fiber-optics to couple light into the UHV, it is possible to host the laser and all the necessary optical components on an optical table that is physically isolated from the UHV system. This allows for effective decoupling of the mechanical vibrations between the optical and AFM systems.

Following the successful integration of the ultrafast laser into the UHV AFM system, it becomes possible to carry-out any optical spectroscopy technique suited to the experiment at hand. The simplest configuration to start with is that of an optical autocorrelator, which allows for a simultaneous measure of the pulse characteristics through optical and AFM detection.

3.3 Autocorrelation of Femtosecond Pulses

The development of laser sources operating in the pico- to femtosecond time domain, and more recently in the sub-femtosecond region, triggered a need for new techniques capable of characterizing ultrafast optical pulses [56]. Optical autocorrelators soon became a favored method for reliably extracting pulse characteristics in cases where pulse widths were too short (< 20 ps) to be directly measured electronically with photodetectors and sampling scopes [57, 58]. This technique, originally proposed and demonstrated by Weber and Armstrong, provides an indirect measure of pulse width by correlating the temporal trace of an ultrafast pulse with itself.

Pulse correlation measurements by second harmonic generation are most often performed in one of two configurations of the optical path: collinear or non-collinear (figure 3.5) [59]. In either case, to perform an autocorrelation the input optical pulse must be divided into two beams, where one beam travels a fixed path, and another a path of variable length. By adjusting the path length of the latter, it is possible to mechanically vary the delay between the pulses. The pulses are subsequently recombined in a nonlinear optical crystal for second harmonic generation. This crystal is specifically selected to have a high second order nonlinear susceptibility $\chi^{(2)}$ and aligned to satisfy phase-matching, so as to ensure efficient SHG over the entire bandwidth of the pulse. The generated second harmonic is subsequently detected as a function of delay time using conventional means (e.g. photodiode). For a more in-depth explanation of the nonlinear processes at hand, please refer to section 4.1.

The experimental configuration and details of the autocorrelation technique are detailed below.

3.3.1 Intensity Autocorrelation

In an intensity autocorrelator (figure 3.5), the two beams are focused in the nonlinear crystal in a non-collinear arrangement, and thus a second-harmonic is not detected if either beam is blocked or the pulses are not temporally overlapped in the crystal [60]. One benefit of this configuration is that the detected 2ω signal is background-free: due to momentum convervation, the fundamental beams are spatially separated from the generated second harmonic.

Following Kaertner's approach and neglecting normalization factors, quasi-phase matching effects, and any z-dependence in the electric field, it is possible to express

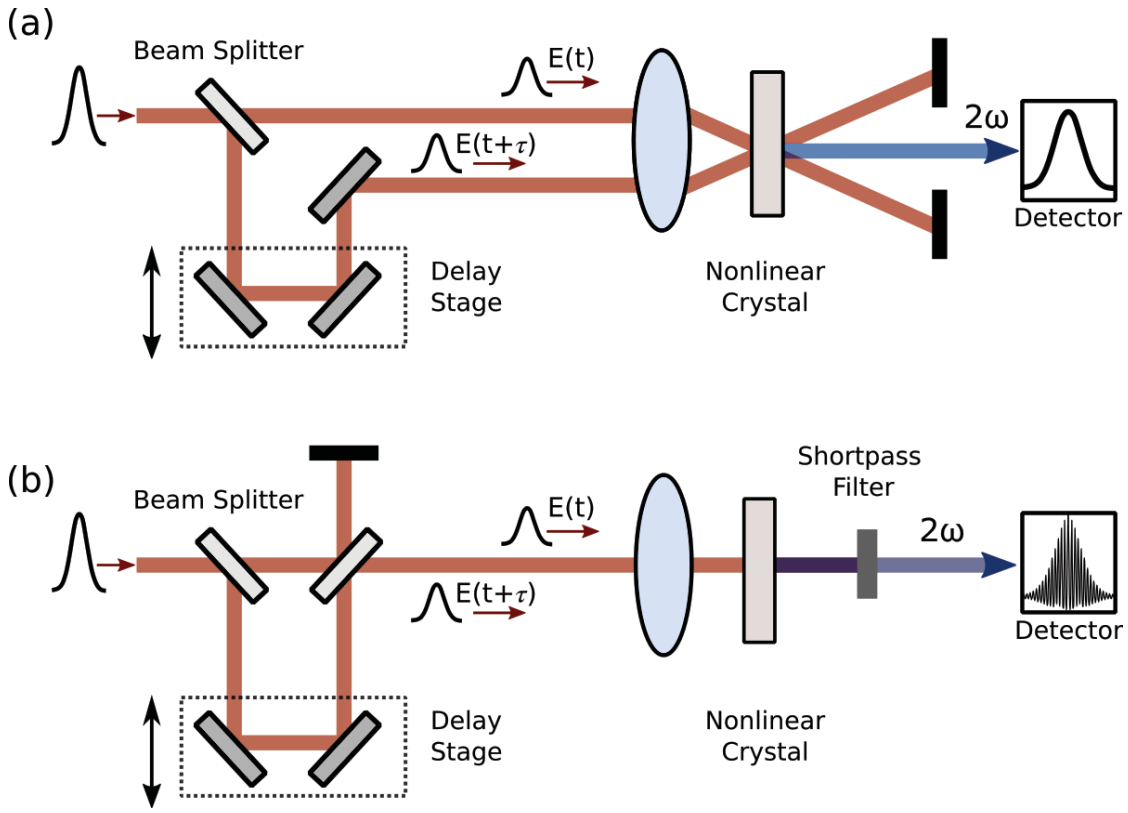

FIGURE 3.5: (a) Intensity and (b) interferometric configurations for pulse correlation measurements by second-harmonic generation. In both arrangements, the input is split in two, and one leg of the beam is delayed with respect to the other. The beams are recombined in a non-linear crystal for second harmonic generation, and this 2ω signal is recorded as a function of time delay. To avoid pulse distortions or dispersion, a thin nonlinear crystal and reflective optics are typically used.

the nonlinear polarization induced in the crystal by the two optical fields $E_1(t)$ and $E_2(t)$ as [61]:

$$P^{(2)}(t) \propto \int_{-\infty}^{\infty} \int_{-\infty}^{\infty} \chi^{(2)}(t-t_1, t-t_2) E_1(t_1) E_2(t_2)\, dt_1\, dt_2 \tag{3.1}$$

Approximating the material response as instantaneous, $\chi^{(2)}$ assumes the form of a Dirac delta-function localized at t_1 and t_2: $\chi^{(2)}(t-t_1, t-t_2) \rightarrow \chi^{(2)}\delta(t-t_1)\delta(t-t_2)$. Thus, the polarization becomes:

$$P^{(2)}(t) \propto E_1(t) E_2(t) \tag{3.2}$$

In the non-collinear configuration (figure 3.5) it is possible to geometrically isolate and eliminate the background, such that the autocorrelation signal completely vanishes when the beams are not overlapped in space and time. Thus, the polarization

simplifies to:

$$P^{(2)}(t) \propto E(t)E(t-\tau). \tag{3.3}$$

The electric field of the generated second harmonic $E(t)$ is directly proportional to the polarization.

Letting $A(t)$ denote the complex envelope of the electric field $E(t)$, then the detected intensity $I(\tau)$ is of the form:

$$I(\tau) \propto \int_{-\infty}^{\infty} \left|A(t)A(t-\tau)\right|^2 dt \tag{3.4}$$

$$\propto \int_{-\infty}^{\infty} I(t)I(t-\tau)\, dt \tag{3.5}$$

Unfortunately, the intensity autocorrelation cannot be used to retrieve any information about the shape or phase of the pulse. With a known pulse shape, it is possible to extract the pulse width using a deconvolution factor. For a Gaussian pulse, for example, the full-width-half-max (FWHM) of the pulse τ_p is related to the FWHM of the intensity autocorrelation τ_{AC} by $\tau_p = \tau_{AC}/\sqrt{2}$

3.3.2 Interferometric Autocorrelation

For an interferometric autocorrelator (figure 3.5), the two pulses are collinearly propagating in the crystal, and thus the fundamental and generated second harmonic are also re-radiated collinearly from the crystal (figure 3.5). A filter can be used to eliminate contributions from the fundamental beam so only the second harmonic is detected.

Once the two pulses have been delayed with respect to each and recombined, the total electric field $E(t,\tau)$ can be represented by:

$$E(t,\tau) = E(t+\tau) + E(t) \tag{3.6}$$

$$= A(t+\tau)e^{i\omega_c(t+\tau)e^{i\phi}} + A(t)e^{i\omega_c t}e^{i\phi}, \tag{3.7}$$

where A(t) is the complex amplitude, ω_c is the carrier frequency, and ϕ the carrier-envelope phase. Following from equation 3.2, and assuming the ideal case in which both beams are truly identical, the polarization can be expressed as:

$$P^{(2)}(t,\tau) \propto \left(A(t+\tau)e^{i\omega_c(t+\tau)e^{i\phi}} + A(t)e^{i\omega_c t}e^{i\phi}\right)^2. \tag{3.8}$$

And following from equation 3.3, we can expressed the radiated electric field of the second harmonic with respect to the polarization:

$$E(t,\tau) \propto \left(A(t+\tau)e^{i\omega_c(t+\tau)e^{i\phi}} + A(t)e^{i\omega_c t}e^{i\phi}\right)^2. \tag{3.9}$$

The intensity recorded by the detection electronics is integrated over the envelope of each pulse, and thus:

$$I(\tau) \propto \int_{-\infty}^{\infty} \left| \left(A(t+\tau)e^{i\omega_c(t+\tau)e^{i\phi}} + A(t)e^{i\omega_c t}e^{i\phi}\right)^2 \right|^2$$

Evaluating the integral and simplifying, the interferometric autocorrelation function assumes the form:

$$I(\tau) = I_b + I_{int}(\tau) + I_{\omega_c}(\tau) + I_{2\omega_c}(\tau), \tag{3.10}$$

where the background signal I_b, the intensity autocorrelation I_{int}, and the coherence terms oscillating with ω_c and $2\omega_c$, I_{ω_c} and $I_{2\omega_c}$, respectively, are given by:

$$I_b = \int_{-\infty}^{\infty} \left(|A(t+\tau)|^4 + |A(t)|^4\right)\, dt = 2\int_{-\infty}^{\infty} I^2(t)\, dt \tag{3.11}$$

$$I_{int}(\tau) = 4\int_{-\infty}^{\infty} |A(t+\tau)|^2|A(t)|^2\, dt = 4\int_{-\infty}^{\infty} I(t+\tau)I(t)\, dt \tag{3.12}$$

$$I_{\omega_c}(\tau) = 4\int_{-\infty}^{\infty} \mathrm{Re}\left[\left(I(t+\tau) + I(t)\right) A^*(t)A(t+\tau)e^{i\omega_c\tau}\right]\, dt \tag{3.13}$$

$$I_{2\omega_c}(\tau) = 2\int_{-\infty}^{\infty} \mathrm{Re}\left[A^2(t)(A^*(t+\tau))^2 e^{i2\omega_c\tau}\right]\, dt \tag{3.14}$$

Note that any dependence on the carrier-envelope phase prove irrelevant given ϕ is the same for both pulses. To reliably extract a pulse width from an interferometric autocorrelation, it is necessary to isolate $I_{int}(\tau)$ and use the fitted width from that term alone. Experimentally this can be achieved by averaging the interferometric trace, or analytically by using Fourier filtering to eliminate the ω and 2ω frequency components. Additionally, it is common to normalize the autocorrelation trace to the background, where $I_{norm}(\tau) = I(\tau)/I_b$. In general, a perfect interferometric autocorrelation exhibits a 1:8 ratio between the background and the peak signal, which occurs at zero delay when both pulses undergo complete constructive interference.

Both intensity and interferometric optical autocorrelators are very useful methods for characterizing femtosecond laser pulses and extracting pulse parameters. As explained in the following chapter, we integrate this technique into our UHV-AFM system to simultaneously retrieve autocorrelation traces both in and out of vacuum.

Chapter 4

Detecting the Second-Order Optical Susceptibility with AFM

Nonlinear optics is the study of how optical properties of a material system can be modified in the presence of intense light. In the traditional case of linear optics, the polarization of the material is proportional to the strength of the incident optical field, where the constants of proportionality are the linear susceptibility $\chi^{(1)}$ and the permittivity of free space ϵ_0. However, for sufficiently intense optical fields or materials with high nonlinear susceptibilities, the polarization response of the material includes higher-order, nonlinear terms as well. In general terms, one can understand this effect by considering the potential energy function $U(x)$ of the nonlinear medium: the electric field of an incident coherent light source will cause the electrons in a medium to oscillate about their potential minimum [62, 63].

In a nonlinear noncentrosymmetric material, such as lithium niobate, the potential energy will deviate from purely parabolic due to the higher-order anharmonic corrections. The motion of the electrons within this material can be described by a classical anharmonic oscillator, for which the driving force is the applied electric field and the restoring force is a nonlinear function of the electron position—-and from this, the nonlinear optical susceptibility emerges. Forces arising from this nonlinear light-matter interaction can be measured using AFM.

Notably, changes in the nonlinear polarization occur according to the response time of the nonlinear susceptibility $\Delta t \sim \hbar/\Delta W$, where ΔW is the nearest resonant transition; typically, Δt is on the order of attoseconds [64]. Thus, changes in the nonlinear polarization occur almost instantaneously, meaning the achievable time resolution in this case is governed by the resolution of the measurement technique. As such, nonlinear optical systems are the perfect test bed for probing the lower-limit of time resolution in AFM. In the following, we explain the relevant nonlinear

processes, further detailing how changes in the nonlinear polarization can be detected by AFM.

4.1 Second-order Nonlinear Mixing

In second order processes, the nonlinear medium acts to produce the sum, difference, or second harmonic of the input field. They are the nonlinear interactions used in our experimental set-up. Following Boyd's approach, we can quantitatively understand the electric field of the impinging optical wave $\tilde{\boldsymbol{E}}(\boldsymbol{r},t)$ as the discrete sum of a number of frequency components [63]:

$$\tilde{\boldsymbol{E}}(\boldsymbol{r},t) = \sum_n \boldsymbol{E}(\boldsymbol{r},\omega_n)e^{-i\omega_n t}, \tag{4.1}$$

where

$$\boldsymbol{E}(\boldsymbol{r},\omega_n) = \boldsymbol{A}(\omega_n)e^{i\boldsymbol{k}_n\cdot\boldsymbol{r}}, \tag{4.2}$$

such that $\boldsymbol{E}(\boldsymbol{r},-\omega_n) = \boldsymbol{E}(\boldsymbol{r},\omega_n)^*$ and $\boldsymbol{A}(-\omega_n) = \boldsymbol{A}(\omega_n)^*$. The nonlinear polarization can be similarly expressed as a sum over the number of frequency components:

$$\tilde{\boldsymbol{P}}(\boldsymbol{r},t) = \sum_n \boldsymbol{P}(\boldsymbol{r},\omega_n)e^{-i\omega_n t}, \tag{4.3}$$

From this we can extract the tensor components of the second-order susceptibility, $\chi^{(2)}_{ijk}(\omega_n+\omega_m;\omega_n,\omega_m)$, to relate the nonlinear second-order polarization to the product of the field amplitudes:

$$P_i(\omega_n+\omega_m) = \epsilon_0 \sum_{jk}\sum_{(nm)} \chi^{(2)}_{ijk}(\omega_n+\omega_m;\omega_n,\omega_m)E_i(\omega_n)E_k(\omega_m), \tag{4.4}$$

where (nm) is used to signify that the sum performed over n and m allows ω_n and ω_m to vary independently, while holding their sum $\omega_n+\omega_m$ fixed. Additionally, the indices ijk are used to indicate the Cartesian components of the fields. All second-order processes, such as sum-frequency generation, difference frequency generation, second harmonic generation, and optical rectification follow from equation 4.4.

We begin with the case of sum-frequency generation, in which two input fields of frequency ω_1 and ω_2, respectively, interact with a nonlinear medium to generate an output field of frequency $\omega_3 = \omega_1 + \omega_2$.

In this case, performing the summation in equation 4.4—-and noting that $\chi^{(2)}_{ijk}$ is symmetric under the interchange of the last two indices—-yields a nonlinear polarization of the form:

$$P_i(\omega_3) = 2\epsilon_0 \sum_{jk} \chi^{(2)}_{ijk}(\omega_3; \omega_1, \omega_2) E_j(\omega_1) E_k(\omega_2) \tag{4.5}$$

Notably, sum- and difference-frequency generation are related by the transformation $\omega_2 \rightarrow -\omega_2$. For the case in which the two impinging fields oscillate at the same frequency ω_1 both these processes occur to yield a second-order polarization comprised of a zero frequency component $(\omega_3 = \omega_1 - \omega_1)$ and a second harmonic component $(\omega_3 = \omega_1 + \omega_1)$. The zero-frequency term follows from equation 4.5 by taking $\omega_2 \rightarrow -\omega_1$ and noting $E(-\omega_n) = E(\omega_n)^*$:

$$P_i(0) = 2\epsilon_0 \sum_{jk} \chi^{(2)}_{ijk}(\omega_3 = 0; \omega_1, \omega_1) E_j(\omega_1) E_k(\omega_1)^* \tag{4.6}$$

The difference frequency generation between two input fields of the same frequency is referred to as optical rectification and results in a static output field.

Second harmonic generation occurs when a nonlinear medium generates an output field of frequency $2\omega_1$ for an input field of frequency ω_1:

$$P_i(\omega_3) = \epsilon_0 \sum_{jk} \chi^{(2)}_{ijk}(\omega_3; \omega_1, \omega_1) E_j(\omega_1) E_k(\omega_1) \tag{4.7}$$

4.1.1 Phase Matching

For nonlinear mixing processes, phase-matching determines which nonlinear interaction will be predominantly observed and occur with the highest efficiency. Phase-matching is a statement of momentum conservation, and requires that the wave-vector mismatch Δk is zero [65]. However, in certain cases perfect phase-matching cannot be implemented—-a notable example being ultrashort pulses, for which achieving $\Delta k = 0$ for all the frequency components is not possible—-and instead quasi-phase-matching must be achieved.

The range of Δk over which the desired process happens with sufficient efficiency is defined as the phase-matching bandwidth, where $|\Delta k| < 2.78/L$ must be satisfied for second-harmonic generation [66]. In typical experiments, the parameter L is

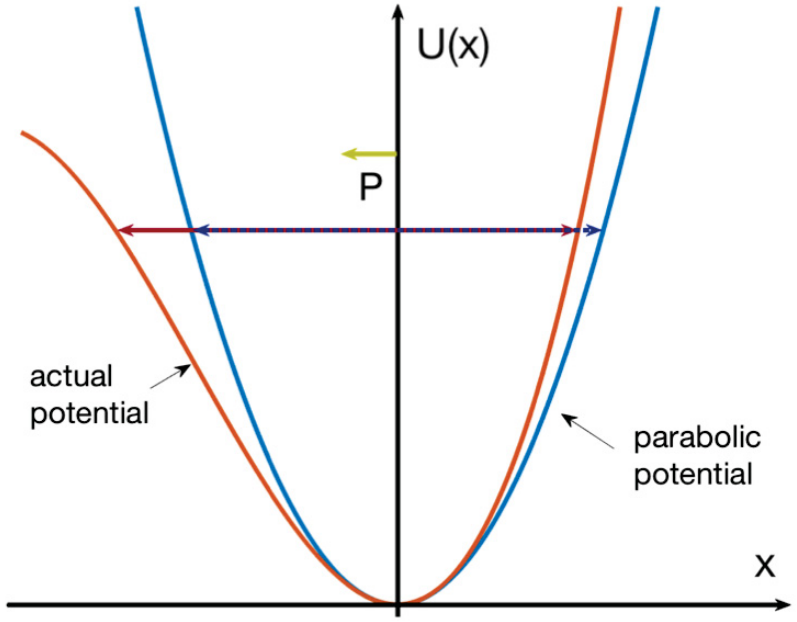

FIGURE 4.1: Potential energy function for a noncentrosymmetric material (orange), for which $U(x) \neq U(-x)$ by definition. The motion of the electrons about the potential minimum, which is driven by the applied electric field, results in a net static polarization referred to as optical rectification. Figure adapted from [63]

defined as the length of nonlinear material through which the light travels. If L is made infinitely small, then phase-matching is always satisfied.

It is worth noting that the AFM tip is only sensitive to the surface of a material; though the penetration depth is not well characterized as yet, it is typically on the order of tens to hundreds of nanometers [67]. This small probe volume means that L is sufficiently small to ensure phase-matching is effectively always satisfied.

4.2 Sensing Polarization Changes with FM-AFM

As detailed in section 2.1, the AFM cantilever can be treated as a damped, driven simple harmonic oscillator. In FM mode, the recorded frequency shift is proportional to the spatial gradient of the tip-sample interaction force. Generally, the tip-sample interactions are comprised of short- and long-range interactions, including contributions from the van der Waals force, chemical forces, and electrostatic forces, amongst others. For our operating conditions and tip-sample distance, the electrostatic force is the dominant force sensed by the tip. Thus, physical processes that result in a detectable electrostatic force can be probed by FM-AFM.

As demonstrated above (equation 4.4), the second-order nonlinear polarization contains frequency components arising from second-harmonic generation, sum- and difference-frequency generation, as well as optical rectification. However, it is not obvious which, if any, of these processes can be sensed by the AFM tip. By modifying the Lorentz model of the atom to include nonlinearities in the restoring force acting on the electron, it is possible to describe the relationship between the AFM and these second-order interactions. The equation of the motion for the electron position $\tilde{x}$ in a noncentrosymmetric medium can be described by the following ODE [62, 63]:

$$\ddot{\tilde{x}} + 2\gamma\dot{\tilde{x}} + \Omega_0^2\tilde{x} + a\tilde{x}^2 = -e\tilde{E}(t)/m, \tag{4.8}$$

where $\tilde{E}$ is the applied electric field, the damping force is $-2m\gamma\dot{\tilde{x}}$, and the parameter a denotes the strength of the nonlinearity. Physically, we can understand equation 4.8 as describing the motion of the electrons oscillating about the potential minimum of a non-parabolic, non-symmetric potential energy function (figure 4.1) of the form:

$$U(\tilde{x}) = \int m\omega_0^2\tilde{x} + ma\tilde{x}^2\, d\tilde{x} = \frac{1}{2}m\omega_0^2\tilde{x}^2 + \frac{1}{3}ma\tilde{x}^3. \tag{4.9}$$

In turn, the electron motion in this potential, induced by the incident laser field, gives rise to a re-radiated electric field that propagates in the direction perpendicular to the electron's direction of motion. This emitted field exerts an electric force on the cantilever and thereby alters its resonance frequency. We can track this change of frequency and relate it directly to a force. It is important to note that the tip cannot sense forces that are acting perpendicular to its direction of motion.

Additionally, the force the cantilever feels from the re-radiated field is time-averaged over the cycle time of the cantilever (a few hundred kilohertz). For a purely parabolic potential, for example, the time average of the re-radiated field would be zero, and thus, a force would not be detected by the cantilever. In the case of an anharmonic potential, as depicted in figure 4.1, the time-average of the re-radiated field is non-zero: the force exerted on the tip arises from the net static polarization, which is referred to as optical rectification (equation 4.6). Thus, the electrostatic force exerted on the tip arises purely from the zero-frequency process of optical rectification; other frequency components arising from a second-order nonlinear interaction cannot be detected via AFM in this configuration.

4.3 Experimental Implementation: Autocorrelation by Optical Rectification with FM-AFM

To probe the zero-frequency term in the second-order nonlinear polarization, we implement a simple autocorrelation scheme to retrieve concurrent measurements of the pulse overlap in air and in vacuum. The autocorrelation in air occurs via second-harmonic generation and is detected using traditional optical methods, while the AFM tip is used to record the pulse overlap in vacuum by using the optically rectified signal from a nonlinear crystal. This experimental scheme is used as proof-of-concept to verify that the force sensing performed by the AFM yields results in agreement with a well-accepted optical technique.

4.3.1 Optical Autocorrelation Scheme

To achieve this, we implement the experimental scheme depicted in figure 4.2. First, we split the output of a mode-locked, P-polarized laser (Toptica FemtoFiber pro NIR) operating at 780 nm (10 nm bandwidth) and 80 MHz using a 50:50 beam splitter (Thorlabs UFBS5050). The generated pulse trains are delayed with respect to each using using two mechanical stages.

A free-space delay stage (Thorlabs ODL220) is used to achieve minimum delays of 0.66 fs, with a full travel range of 1466 ps. To introduce finer delays (sub-1 fs), two fused-silica wedges (Newlight Photonics QAR15121-A4-AR800/400) are used in conjunction: one wedge is mounted on a translation stage and slowly moved into the beam path, while the other is held fixed. The coarser mechanical steps used to move the wedge are thus converted into optical delays of a few tens of attoseconds through the relationship [68]:

$$\Delta\tau = \Delta\ell(1-n)\frac{\tan(\alpha)}{c}, \tag{4.10}$$

where $\Delta\tau$ is the temporal delay, $\Delta\ell$ the step size of the mechanical stage, and c the speed of light in air.

The two pulse trains are subsequently recombined using a 50:50 beam splitter: half the recombined beam is directed towards an optical autocorrelator, the other half towards the tip-sample junction in the UHV-AFM. The interferometric optical autocorrelator is comprised of several components: first, a zero-order half-wave plate (WPH05M-780) that rotates the linear polarization of the beam by 90°; second,

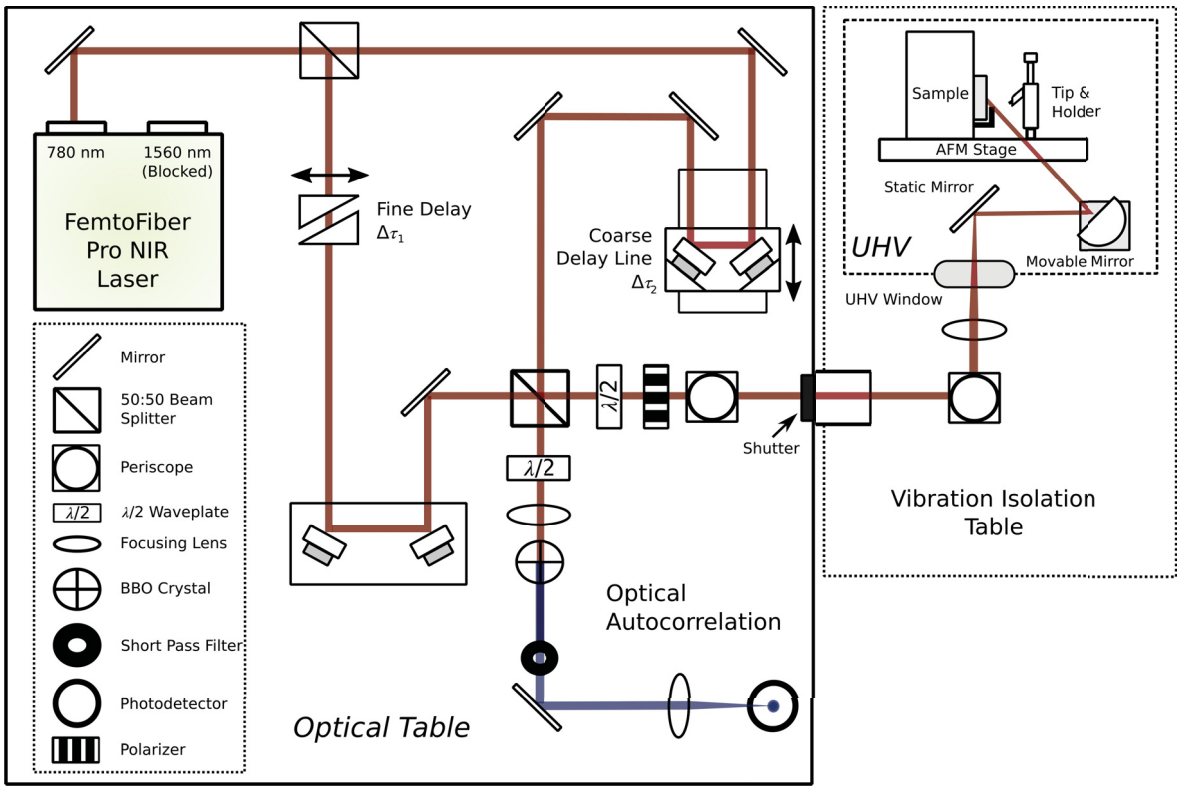

FIGURE 4.2: Schematic of the optical system. The output of a mode-locked 780 nm femtosecond fiber laser is split to produce two identical pulse trains. Coarse and fine delay stages introduce a well defined temporal separation between the pulses. The beams are recombined spatially and simultaneously directed towards the optical autocorrelator, as well as the tip-sample junction in the AFM.

a lens for collinearly focusing the beams in the nonlinear crystal; and third, an ultrathin ($< 100\ \mu$m) BBO (beta borium borate) nonlinear crystal for second-harmonic generation. A short pass filter (Thorlabs FES0450) is used to isolate the 2ω light from the ω beam, and a second lens focuses the 2ω for detection. As the relative time delay is increased, the intensity of the generated 2ω beam goes to zero; conversely, the intensity is at a maximum when the relative delay is zero.

4.3.2 Incorporation into AFM

As previously mentioned, the other leg of the recombined beam is directed towards the AFM stage, which houses our nonlinear sample of choice: PPLN. A half-wave plate is used to orient the polarization of the incident light such that the force exerted by the induced polarization in the sample—in this case, lithium niobate—is along the tip's direction of motion. When the polarization is oriented in this way, the force felt by the AFM tip is maximal. This alignment is therefore quite critical for ensuring good signal-to-noise for AFM measurements.

A calcite polarizer is placed after the wave plate, and together the wave plate and polarizer can be used as a variable power attenuator. The orientation of the polarizer is held fixed as the angle of the wave plate is varied—this ensures the polarization entering the AFM is constant, while allowing for controlled attenuation of the power. Specifically, a rotation by ϕ degrees of the half-wave plate results in a rotation of 2ϕ of the polarization; accordingly, the intensity of the beam after the polarizer is given by $I = I_0 \cos^2(2\phi)$. The output power varies from a maximum to minimum over a 45° rotation of the wave plate.

It is worth nothing that the polarizer causes significant dispersion, and thereby broadens the pulse width—this means that the pulse width in the AFM will be larger than that of the optical autocorrelation. Specifically, dispersion causes the frequency components of an ultrashort pulse to propagate with different velocities, and thereby results in an overall broadened pulse width. The GVD is defined as:

$$GVD = \frac{\lambda^3}{2\pi c^2}\left(\frac{d^2 n}{d\lambda^2}\right) = D_2/L, \tag{4.11}$$

where λ is the wavelength of the propagating light, n the index of refraction of the material, and D_2 the group delay dispersion (GDD); the GVD is the GDD per unit length. After propagating through a dispersive medium, the pulse duration is increase to:

$$\tau = \tau_0 \sqrt{1 + \left(\frac{4\ln(2) D_2}{\tau_0^2}\right)^2}, \tag{4.12}$$

where τ_0 is the pulse duration before dispersive effects.

Two periscopes are used to direct the beam into the UHV at the correct height and angle. The orientation of the second periscope is particularly crucial, as it is last piece of optics we can control before the beam enters the UHV system. This periscope must be carefully aligned such that the beam deflects off the static mirror to impinge perfectly on the center of the movable mirror, which was described in detail in section 3.2.2. An infrared camera is directed towards the movable mirror to serve as a visual guide. Once this alignment has been achieved, the movable mirror can be controlled externally to align the beam to the tip-sample junction. From there, the same feedback scheme used for normal FM-AFM operation (section 2.1) can be implemented for force sensing (figure 4.3). The AFM tip can thereby detect any light-matter interactions resulting in a measurable force.

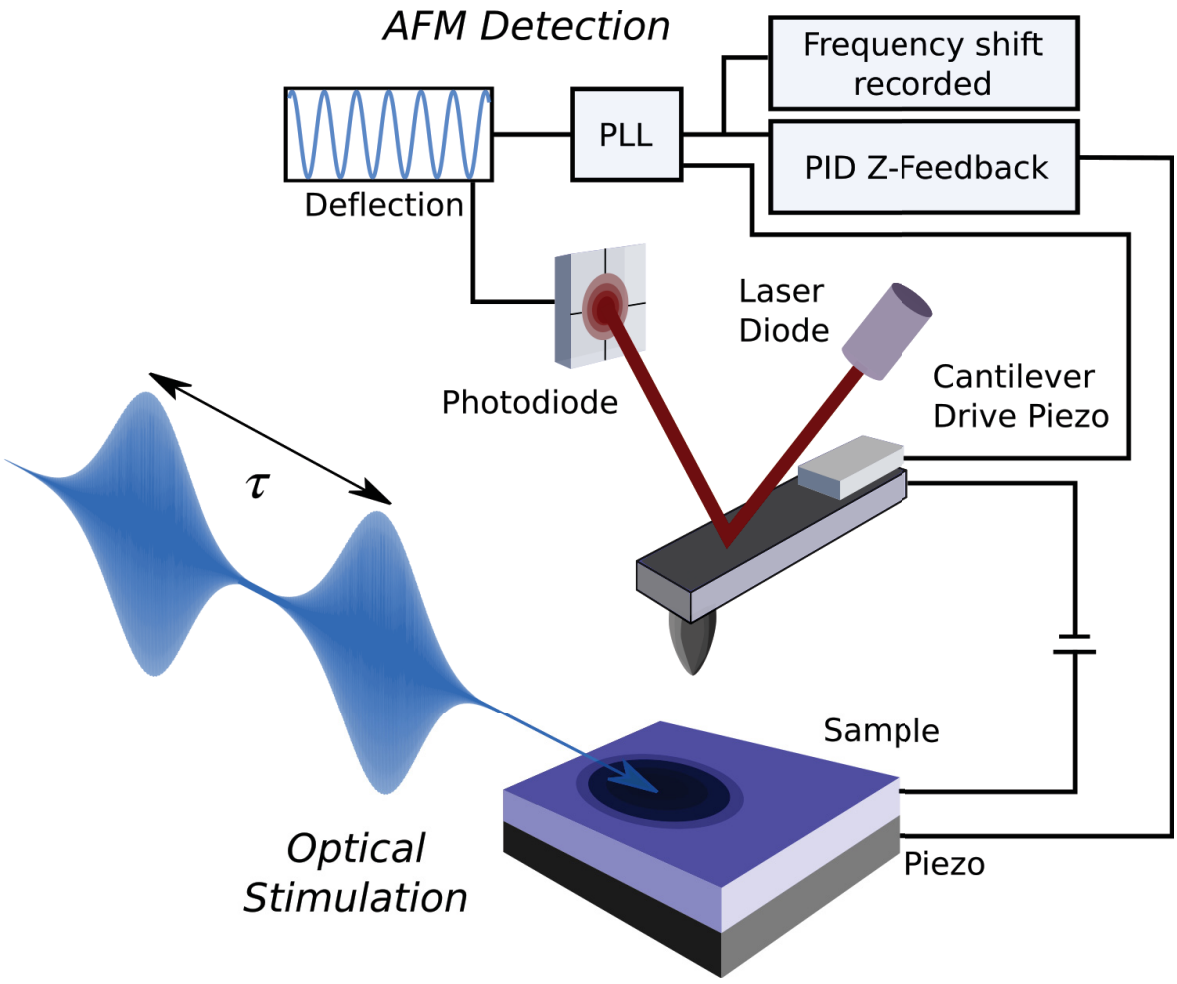

FIGURE 4.3: Two pulses, separated by a temporal delay τ, incident on the sample surface. The angle of incidence of the beams is roughly 80°. The laser light is oriented to hit the tip-sample junction, while ensuring thermal heating of the cantilever does not occur. The AFM tip is used to detect any forces generated by the light-matter interaction using the usual feedback scheme.

Beam Alignment on the Sample Surface

The alignment of the beam on the sample surface is rather sensitive: first, we must ensure both pulse trains are perfectly spatially overlapped on the sample surface; second, the beam must be oriented to guarantee no thermal heating of the cantilever while still exciting the tip-sample junction. Thermally driving the cantilever will introduce measurement artifacts and undermine the stability of the AFM. The coarse alignment of the beam on the sample surface is achieved by visually tracking the laser spot and roughly orienting it around the the tip. The frequency shift is another good measure for rough alignment: a maximal change in the frequency shift is achieved when the light is directly hitting the tip-cantilever ensemble—unfortunately, this also means the cantilever is being thermally driven by the optical field. To remedy this, fine alignment of the beam position is required.

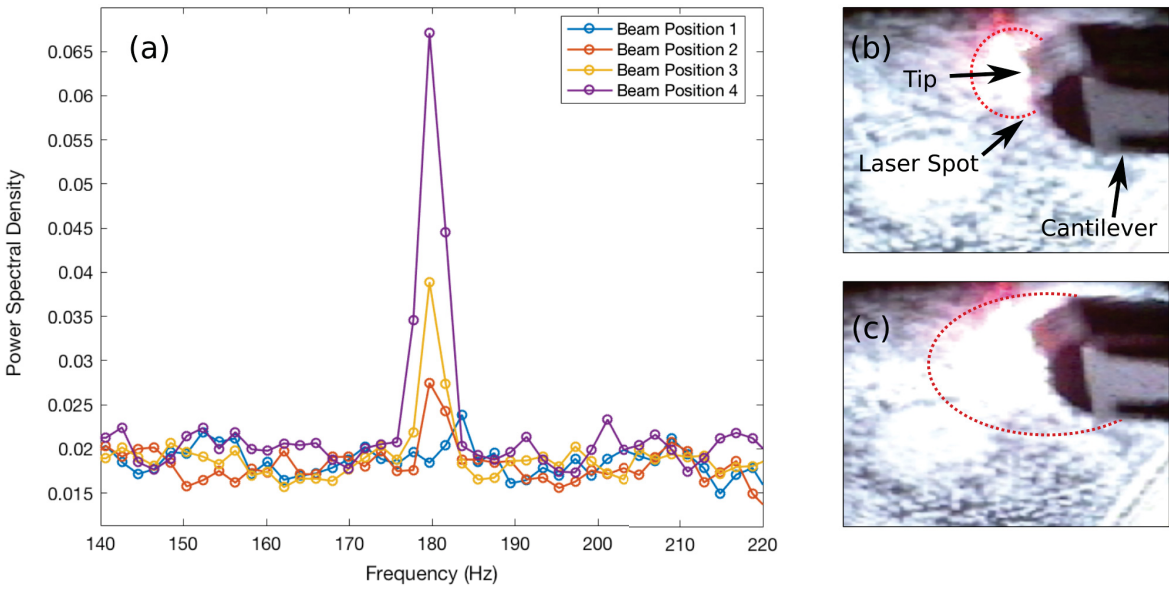

FIGURE 4.4: Thermal heating of the cantilever as a function of the laser spot position on the sample surface. (a) A mechanical chopper at 180 Hz is used to modulate the incident optical field. The power spectral density for four different beam positions is shown. There is a distinct peak at 180 Hz for positions 2-4; the amplitude of the peak corresponds to the amount of induced thermal heating. The power spectral density for position 1 indicates good alignment (i.e. no thermal heating). (b) Infrared camera view of beam position 1 on the sample surface; the laser spot and cantilever are indicated. (c) Beam position 4. As the beam is moved to the right of the tip, thermal driving of the cantilever decreases.

To eradicate any thermal heating of the cantilever, it is first necessary to develop a reliable technique to determine if, and how much, the laser is driving the cantilever. An easy way to accomplish this is to place a mechanical chopper in the path of the incident beam to modulate the excitation at a relatively slow frequency ($\sim$ hundreds of hertz). If the cantilever is being thermally heated, the power spectral density of the tip response will show a peak at the modulation frequency. As the beam is re-positioned, the amplitude of this peak will increase or decrease based on the amount of thermal heating induced in the cantilever, as shown in figure 4.4. The ultimate aim of the fine alignment is to ensure there is no peak at the modulation frequency when the cantilever is not in tip-sample contact, while ensuring the optical field remains incident on the tip-sample junction. There are more careful measures for optimizing the alignment even further; these will be discussed in further detail in the following chapter.

Interferometric versus Intensity Autocorrelation

The choice between integrating an interferometric or intensity autocorrelator into the AFM is non-obvious. For optical detection, the difference between these two techniques is negligible: both trace the overlap of the pulses to yield a measure of the pulse width. However, the collinear or non-collinear configuration associated with each technique has significant impact on measurements performed via AFM.

We implement both autocorrelation schemes to determine which is better suited for our application. As mentioned above, both beams must be focused to the same spot on the sample surface. Requiring perfect spatial overlap is easily achieved when a collinear (interferometric) set-up is implemented. On the other hand, in a non-collinear (intensity) configuration, maintaining alignment for the optical autocorrelation while achieving spatial overlap at the sample surface is very challenging. This is an important disadvantage because it is imperative to be able to successfully measure the optical and AFM autocorrelation simultaneously.

The other main consideration is the stability of the AFM. In a collinear arrangement, the beams interfere to produce oscillations in the overall intensity as function of delay (figure 3.5). These oscillations significantly perturb the AFM cantilever, making it very difficult to get sufficient signal-to-noise while ensuring the cantilever is not being thermally driven. Ultimately, this makes the AFM detection less stable, even if the alignment is very carefully carried out. To get maximal signal-to-noise in the frequency shift signal, to maintain a constant tip-sample distance, and to ensure there is no cross-talk from the z-controller in Δf, it is necessary to lift the tip from the surface by a set amount ($\sim$1 nm), turn off the z-feedback, and then carry out the measurement. In a collinear optical set-up, this is not possible. Intrinsic instabilities in the interferometric autocorrelator produce low frequency background noise, which makes it unfeasible to perform measurements with the z-feedback turned off. Conversely, a non-collinear set-up does not produce these intensity oscillation as a function of delay time, and thereby helps preserve the stability of the AFM. Measurements taken with the z-feedback off are possible in this case.

Depending on the sample and experiment in question, the above-stated advantages and disadvantages may become relevant. In the experiment presented in the following chapter, most measurements are performed with a collinear optical arrangement.

Chapter 5

Ultrafast Nanoscale Measurements of Optical Rectification in PPLN

Resolving ultrafast physical phenomena on the nanoscale has been a driving force in the development of time-resolved scanning probe techniques. The aim of combining conventional, well-developed optical spectroscopy techniques with equally mature nanophysics methods is simple: to understand the light-matter interactions governing the atomic world. The physics that occurs when ultrafast pulses are used to excite nanosystems is largely ill-understood. To date, most ultrafast optical methods have been devoid of the spatial resolution needed to study physics occurring at the nanometer length scale. Here, we incorporate a pulsed laser system into a UHV-AFM to study ultrafast changes in the electric polarization of a nonlinear crystal occurring at nanometer length-scales.

Our measurement scheme is based on autocorrelation by optical rectification: two coherent pulse trains are temporally separated by a well-defined delay and collinearly focused on a nonlinear crystal with a strong second-order susceptibility, in this case periodically poled lithium niobate (PPLN). In turn, the incident light gives rise to a second-order polarization change in the sample that follows the electric field of the impinging $\sim$100 fs laser pulses. The electrostatic force originating from this induced polarization change in lithium niobate is detected and spatially resolved using non-contact AFM. Below we discuss our results and provide further characterization of our ultrafast AFM technique.

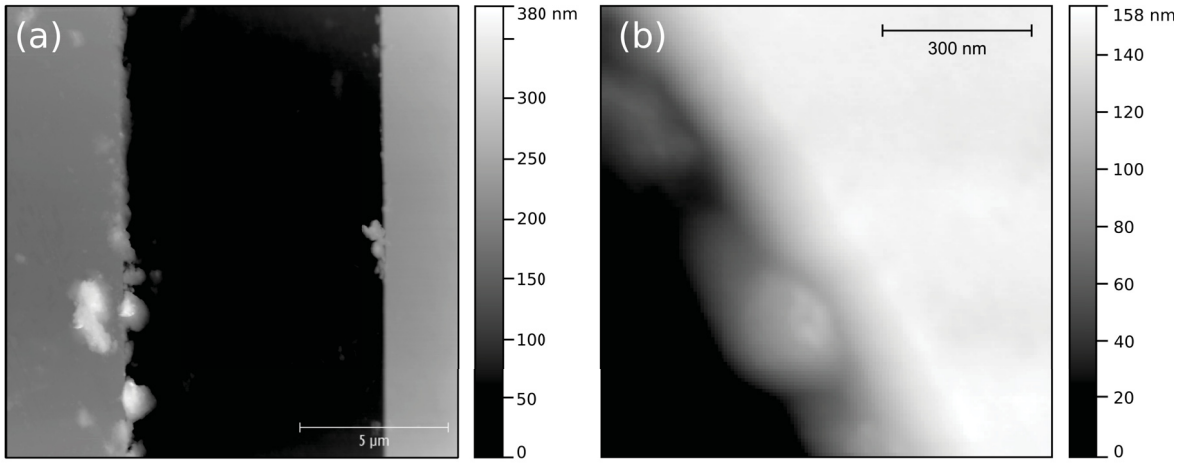

FIGURE 5.1: Topographical image of the sample surface. (a) Tapping mode image of surface domains, which have a poling periodicity of 8.5 μm. (b) Non-contact mode image (f_0=304.2 kHz, Q = 19285, A_0=6 nm) of a step edge over one domain boundary. The frequency shift set point is at -3 Hz and a bias of 4.51 mV is applied to compensate the potential difference between tip and sample is applied. Surface adsorbents and impurities are clearly visible in both topographical maps.

5.1 Results & Discussion

We implement the experimental set-up detailed in section 4.3 to couple the optical field of two pulse trains to the tip-sample junction. Our measurement scheme allows us to vary the delay τ between the two pulses while concurrently retrieving data using both the optical autocorrelator and the AFM. Using the same principle on which optical autocorrelators were founded, we use a nonlinear crystal (z-cut, HF-etched PPLN) to transform the input fields into an optically rectified, zero-frequency polarization that results in a force which we measure using FM-AFM.

Upon coupling the light to the tip-sample junction, we approach a metal coated silicon tip (Nanosensors, PPP-NCHPt, f_0=304.2 kHz, Q = 19285) to the sample surface. We characterize the PPLN surface using AFM (figure 5.1) to determine: the poling periodicity is 8.5μm; step edges over domain boundaries host large aggregates of unknown surface adsorbents and impurities; and the HF-etching has introduced a $\sim$ 160 nm height difference between the poling regions. The reverse poling of the lithium niobate thus corresponds to the topography.

We move the tip slightly closer to the surface (frequency shift set point of -15 Hz) for better signal-to-noise, and subsequently vary the delay between the two pulses while simultaneously recording the read-out from the photodiode (for optical detection) and the measured frequency shift (for FM-AFM detection). The proportional

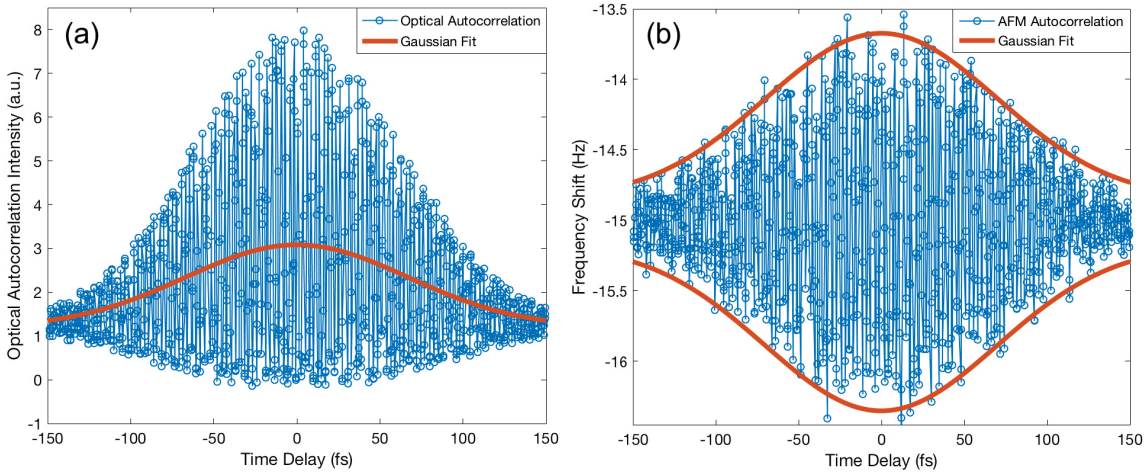

FIGURE 5.2: Autocorrelation traces retrieved concurrently using optical and AFM detection methods, respectively. (a) Optical interferometric autocorrelation signal. An FFT filter is applied to extract the intensity autocorrelation component (red), the Gaussian fit for which yields a pulse width of 111±10 fs. (b) Measured frequency shift, arising from an induced polarization change in PPLN, as a function of delay time between the two incident pulses. A pulse width of 116±6 fs is extracted. The power of both input fields is 6.56 mW. Four data points are taken at each delay step, with 20 ms integration time per point. A Gaussian pulse profile is assumed in both cases.

gain of the z-feedback loop is significantly decreased from normal operational values to ensure the feedback is slow enough to allow changes in the frequency shift to be detected; all the measurements obtained with the z-feedback activated are taken with a p-gain of 10 pm/Hz.

The interferometric optical autocorrelation occurs via second-harmonic generation and exhibits the ideal 8:1 ratio characteristic of good optical alignment (figure 5.2). The extracted pulse width is 111±10 fs, in agreement with our laser specifications. The corresponding AFM autocorrelation (figure 5.2) yields a pulse width of 116±6 fs. The discrepancy in pulse widths is due to additional dispersion accrued from the calcite polarizer, focusing lens, and UHV window. The dispersion can be calculated using equation 4.12, resulting in an expected broadening of 4 fs for an input pulse of width 111 fs.

The AFM autocorrelation traces the force gradient arising from the second order polarization

$$P^{(2)}(t) = \epsilon_0 \chi^{(2)} E(t) E^*(t+\tau) e^{-i\omega_0 \tau}, \tag{5.1}$$

which oscillates with respect to the delay time τ with a period of $2\pi/\omega_0$, where ω_0 is the carrier frequency. The oscillations predicted by equation 5.1 can be well resolved experimentally. Figure 5.3 shows measurements of the single-cycle oscillations of the electrostatic force arising from the nonlinear mixing. The sensitivity of the AFM

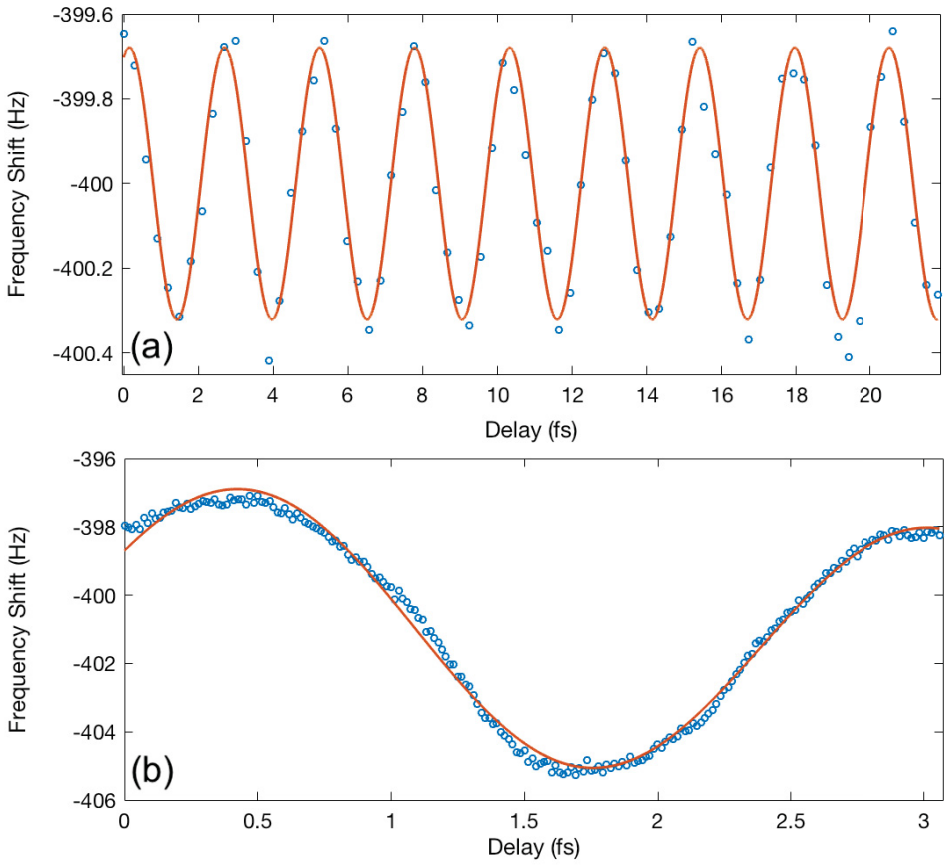

FIGURE 5.3: Single-cycle oscillations of the optically rectified field. The delay is finely stepped and the frequency shift response (blue) is recorded; the data is fitted (orange) to a sinusoid with a period of 2.6 fs (780 nm). The same measurement is performed with (a) the coarse delay stage, using a minimum step size of 0.6fs and (b) the wedge-pair delay scheme, with a step size of 25 as. Unlike all other measurements presented in this thesis, the high degree of stability needed to perform this particular measurement necessitated using a non-collinear optical configuration; both (a) and (b) are performed with the z-feedback off.

is high enough to distinctly resolve two data points 25 as apart.

Since lithium niobate is an insulator with a bandgap of 3.78 eV, we expect that the input optical field at 1.59 eV does not generate any charge carriers [69]. The observed signal must thereby arise from induced changes in the polarization of the sample. To verify this, we must first exclude the possibility that the observed effect is due to tip artifacts; and furthermore, we must prove it is the polarization change in the sample—and not some other physical phenomenon—that we are detecting.

To this end, we repeat the measurement presented in figure 5.2 several times, and with each iteration vary the polarization of the input field by a controlled amount (figure 5.4). We repeat the measurement on either side of the domain edge, which we refer to as the top and bottom terrace, respectively. In both cases, the intensity of the frequency shift response varies with the polarization, even though the power

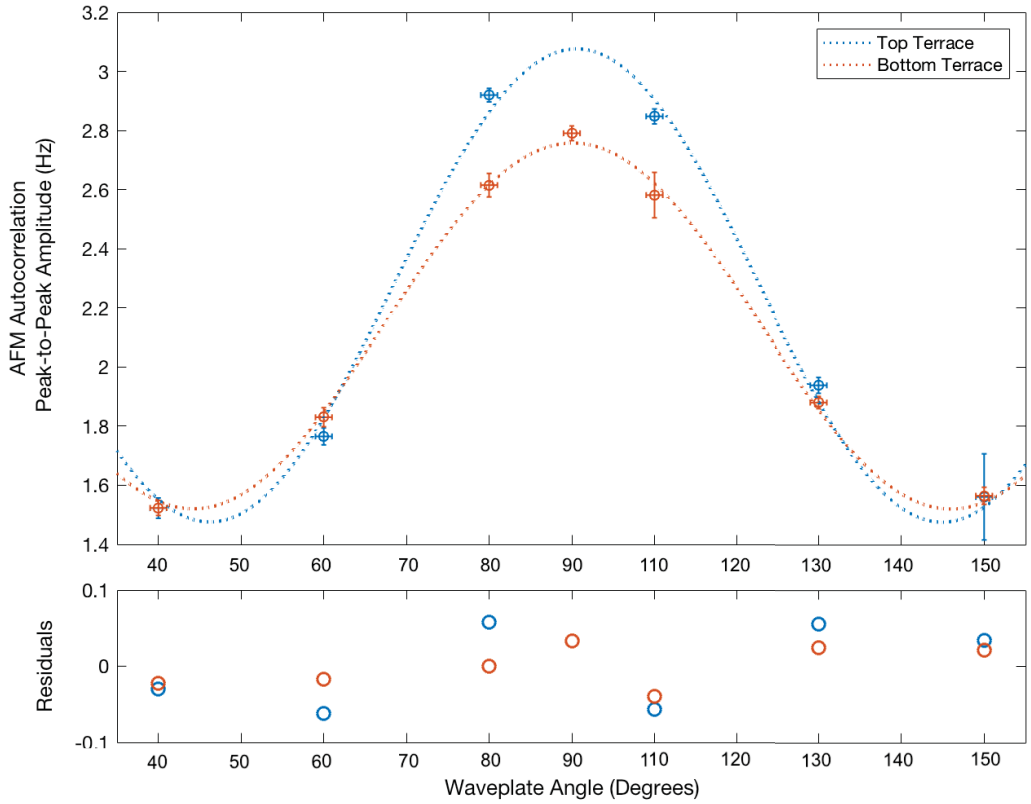

FIGURE 5.4: The peak-to-peak amplitude of the AFM autocorrelation signal is plotted as a function of the half-wave plate angle (points) for constant input power (8.13 mW). In this case, the angle is defined with respect to the fast axis. The peak-to-peak amplitude of the signal is analogous to the intensity of the observed response. As expected, the intensity varies sinusoidally as a function of the wave plate angle, further verified by the fit (dotted lines) and residuals.

entering the AFM stays constant. This indicates the signal originates from the sample, and is not a by-product of thermal driving of the cantilever. Notably, the AFM autocorrelation amplitude never goes to zero as the polarization of the input optical field is varied. One possible explanation for this is geometric: our set-up does not allow the polarization of the input field to be perfectly parallel or perpendicular to the sample plane. Thus, there is always a component of the force along the direction of motion of the tip, indicating there will always be a non-zero signal intensity.

Additionally, from equation 5.1 we expect that the magnitude of the second-order polarization scales with the power of the input field. To probe this dependence in our system, we slowly rotate the polarizer to attenuate the input power (section 4.3.2) without changing the position of the laser spot on the sample. Since the

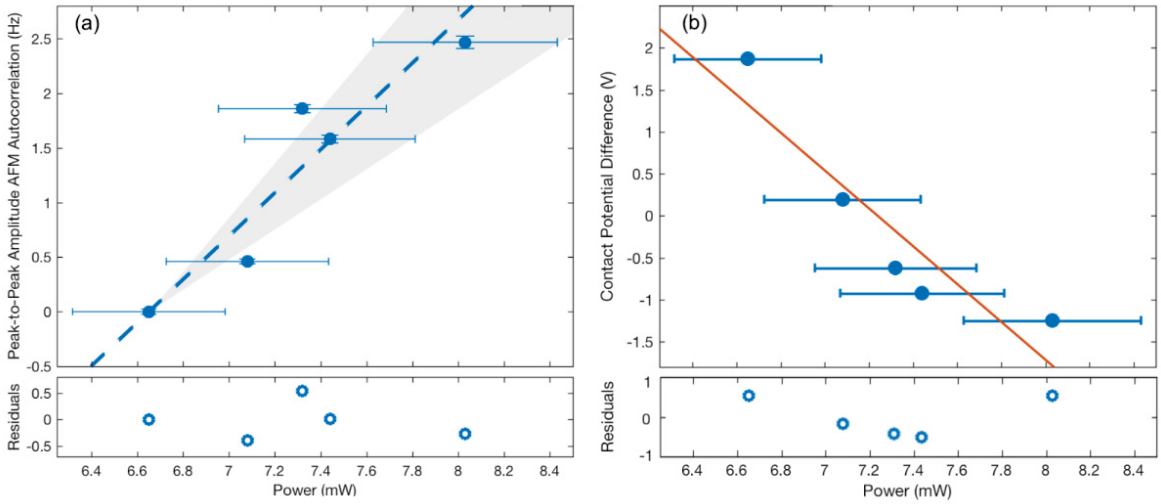

FIGURE 5.5: Power dependence of the polarization response in PPLN. (a) The peak-to-peak amplitude of the AFM autocorrelation (points) as a function of input power. The linear fit (dotted line) and error in the fit (gray area) are indicated. (b) The contact potential difference between the tip and sample (points) as a function of input power, fitted to a linear function (solid line). There is no structure in the residuals for both (a) and (b).

polarizer was rotated relative to the wave plate, there is a slight variation in polarization as well. At each power we measure the contact potential difference (CPD)—-which arises from a work-function difference between the tip and sample—-and nullify this electrostatic force by applying a voltage with the same magnitude, but opposite direction. Afterwards, we concurrently record an AFM and optical autocorrelation. We extract the peak-to-peak amplitude of the AFM autocorrelation and plot it against the input power (figure 5.5). As expected, we observe a linear relationship between power and detected force. Given the limited power range over which measurements are taken, we compare the goodness-of-fit of a linear dependence to that of a quadratic and exponential dependence. The linear fit emerges as the best fit.

Experimental factors limit our available power range to roughly 1 mW: at powers higher than ∼8 mW, the cantilever is subject to thermal heating; at powers less than ∼6.5 mW, the polarization signal is no longer detectable. This limitation only arises in this measurement scheme, for which we keep the position of the beam constant as the power is varied for experimental consistency. In general, operation at higher or lower powers is possible, as long as the beam position relative to the tip is allowed to vary to prevent thermal heating of the cantilever, while also ensuring a detectable signal. The position of the laser spot is critical: the intensity profile of the beam follows a Gaussian distribution, thus, moving the beam relative to the tip changes the effective power experienced by tip-sample junction, even though the input power is

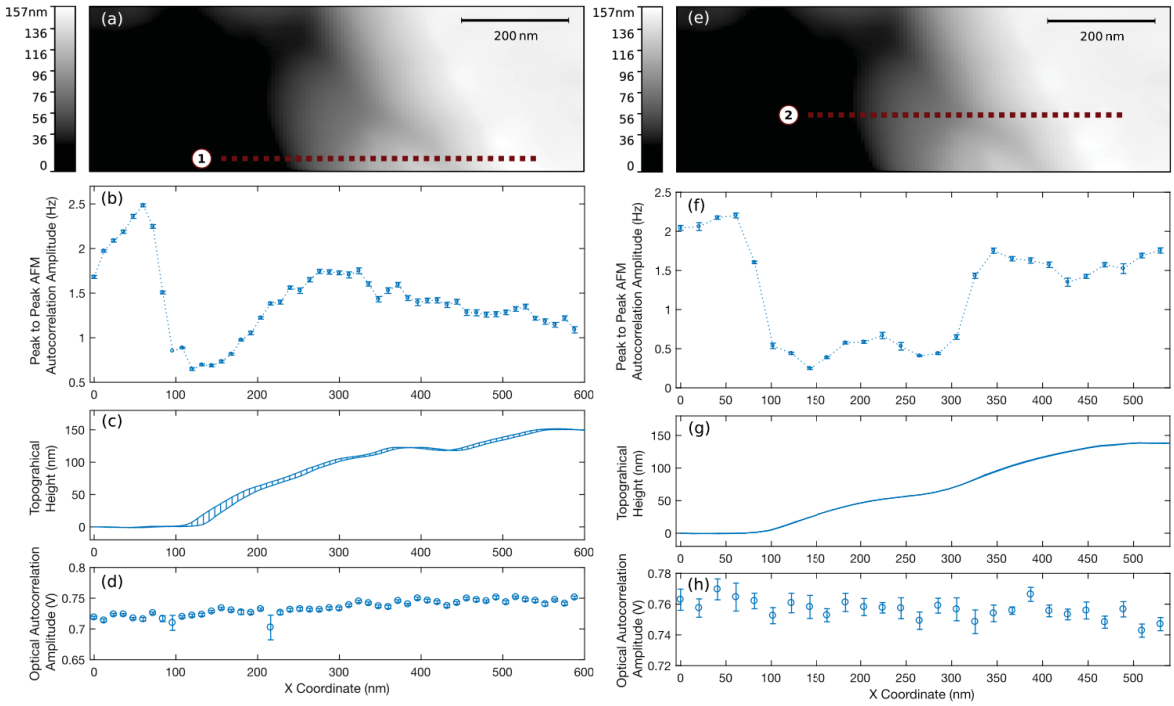

FIGURE 5.6: Nanoscale spatial resolution. (a), (e) Surface topography over the region of interest with the line scan position (red dotted line) overlaid. The imaged domain boundary shows the top terrace (right) and bottom terrace (left), with the edge decorated with surface adsorbents and impurities. (b), (f) Peak-to-peak amplitude of AFM autocorrelation as a function of the tip position, for a total input power of 6.56 mW and step interval of (b) 12 nm and (f) 20 nm. As the tip moves over the surface impurity, the intensity of the AFM autocorrelation approaches zero. (c), (g) Surface topography over the measurement range. (d), (h) Corresponding amplitude of the concurrently retrieved optical autocorrelation.

nominally the same. Taking advantage of this, while continuing to ensure thermal heating is not occurring, allows for operation using a wide range of powers.

Figure 5.5 also shows the CPD variation as a function of power. A linear dependence similarly proves to be the best fit in this case. To understand the underlying physics, we consider the electrostatic force between the tip and sample (equation 2.12), which depends quadratically on the total tip-sample potential. Typically, the extremum of this parabola is the CPD. However, a polarizable medium causes the addition of a charge induced dipole barrier term to the total potential, in effect shifting the extremum of the potential; in this case, the CPD varies linearly with polarization changes [70]. Thus, the power dependence of the AFM autocorrelation intensity and the CPD are in agreement with each other, and further verify the the AFM autocorrelation signal originates from polarization changes in the sample.

Finally, the most convincing piece of evidence to prove the signal arises from the sample lies in corroborating the topography of the surface to the measured force. To this end, we perform a line scan measurement (figure 5.6): first, we nullify the CPD

to reliably map the surface topography over the region of interest, doing so in normal FM-AFM mode (f_0=-2 Hz, bias=3.521 V); at a well-defined point on the sample, we approach the tip slightly closer to the surface (f_0=-15 Hz) to perform an AFM and optical autocorrelation concurrently; we move the tip relative to the sample by a set amount while maintaining f_0=-15 Hz, and repeat the AFM and optical autocorrelation measurement. We are thus able to corroborate the surface topography with the intensity of the nonlinear polarization response. The simultaneously retrieved optical autocorrelation serves as a reference for comparing two AFM measurements taken at different times 1) to ensure the laser alignment has not changed and 2) to account for power fluctuations.

As shown in figure 5.6, we are able to resolve changes in the nonlinear polarization occurring on the nanometer scale. In both line scans, the polarization response approaches zero intensity when measurements are performed over the surface adsorbent on the edge of the domain boundary. Though the identity of this impurity is unknown, this effect is likely due to the impurity effectively attenuating the re-emitted electric field of the underlying lithium niobate. It is important to emphasize that we are able to reliably observe the same trends for different line scan measurements performed over the same region of interest on the surface, demonstrating the method is robust. The concurrently recorded optical autocorrelation measurement shows little variation for both line scans, indicating the stability of the interferometer is good enough for easy comparison of long-time measurements.

Chapter 6

Conclusions & Outlook

In this work, we demonstrate the capabilities of an ultrafast AFM with nanoscale spatial resolution and attosecond temporal precision. We incorporate an ultrafast mode-locked laser into a commercial UHV-AFM system, and implement an optical autocorrelation set-up to perform simultaneous measurement of the pulse overlap in and out of vacuum via optical rectification and second harmonic generation, respectively. We exploit the spatial resolution intrinsic to AFM to resolve the magnitude of the local electrostatic force that arises from an induced change in the nonlinear polarization—-and is quantified through the intensity of the AFM autocorrelation—-as a proof-of-concept of our ultrafast AFM. We demonstrate the reproducibility and robustness of this technique by successfully corroborating the topography with the measured electrostatic force over different line scans.

The presented technique can be extended to measure a host of light-matter interactions happening on the ultrafast nanoscale, such as the χ^2 response of any nonlinear material; and more generally, any optically instigated change which amounts to a detectable force—including, for example, a change in dielectric constant, photocarrier generation and decay, or electron motion. Gaining access to ultrafast physics on atomic length scales opens the door to heretofore unexplored physics. Notably, the optical excitation can take any form—-traditional optical spectroscopy techniques can be implemented, with the AFM tip acting as force sensor in place of a photodetector. The wide applicability of this technique is what makes it powerful.

Semiconductor systems, thin-film organic photovoltaics, or transition metal dichalcogenides are perfect material systems for taking advantage of the capabilities of an ultrafast AFM. Transition metal dichalcogenides, for example, are 2D semiconductors with atomic-scale thickness. Their band structure varies depending on the number of monolayers comprising the material system, shifting from a direct band-gap at one monolayer, to indirect at two. The physics governing these sample properties would be well elucidated by spatially and temporally characterizing the excitonic

and free-carrier dynamics as a function of sample thickness—-a task well suited to the ultrafast AFM. This is only one example of the usefulness of a technique that can probe nanoscale physics on ultrafast time scales.

Ultimately, the development of an ultrafast AFM is an exciting step towards uncovering new physics, and expanding the capabilities of scanning probe techniques in the time domain.

Bibliography

[1] M. Peplow. Peplow, Nature, The next big hit in molecule hollywood. *Nature*, 544(27 April 2017):408, 2017.

[2] H. Mashiko, K. Oguri, A. Yamaguchi, T.and Suda, and H. Gotoh. Petahertz optical drive with wide-bandgap semiconductor. *Nature Physics*, 12(8):741–745, aug 2016.

[3] A. Schiffrin, T. Paasch-Colberg, N. Karpowicz, V. Apalkov, D.l Gerster, S. Mühlbrandt, M. Korbman, J. Reichert, M. Schultze, S. Holzner, J. V. Barth, R. Kienberger, R. Ernstorfer, V. S. Yakovlev, M. I. Stockman, and F. Krausz. Optical-field-induced current in dielectrics. *Nature*, 493(7430):70–74, dec 2012.

[4] A. E. Gildemeister, T. Ihn, C. Barengo, P. Studerus, and K. Ensslin. Construction of a dilution refrigerator cooled scanning force microscope. *Review of Scientific Instruments*, 78:013704, 2007.

[5] T. R. Albrecht, P. Grütter, D. Horne, and D. Rugar. Frequency modulation detection using high-Q cantilevers for enhanced force microscope sensitivity. *Journal of Applied Physics*, 69:668–673, 1991.

[6] T. Ando, T. Uchihashi, and T. Fukuma. High-speed atomic force microscopy for nano-visualization of dynamic biomolecular processes. *Progress in Surface Science*, 83:337–437, 2008.

[7] T. Ando. High-speed atomic force microscopy coming of age. *Nanotechnology*, 23:062001, 2012.

[8] F Xia, T Mueller, Y Lin, A Valdes-Garcia1, and P Avouris. Ultrafast graphene photodetector. *Nature Nanotechnology*, 4:839, 2009.

[9] A Urich, K. Unterrainer, and T Mueller. Intrinsic Response Time of Graphene Photodetector. *Nano Letters*, 11:2804, 2009.

[10] R. J. Hamers and David G. Cahill. Ultrafast time resolution in scanned probe microscopies. *Applied Physics Letters*, 57(19):2031–2033, 1990.

[11] R. J. Hamers and D. G. Cahill. Ultrafast time resolution in scanned probe microscopies: Surface photovoltage on si(111)-(7x7). *Journal of Vacuum Science & Technology B: Microelectronics and Nanometer Structures*, 9:514, 1991.

[12] M Takihara, M. Takahashi, and T. Ujihara. Minority carrier lifetime in polycrystalline silicon solar cells studied by photoassisted kelvin probe force microscopy. *Applied Physics Letters*, 93:021902, 2008.

[13] G. Shao, M. S. Glaz, F. Ma, H. Ju, and D.S Ginger. Intensity-modulated scanning kelvin probe microscopy for probing recombination in organic photovoltaics. *ACS Nano*, 8:10799–10807, 2014.

[14] D. C. Coffey and D. S. Ginger. Time-resolved electrostatic force microscopy of polymer solar cells. *Nature Materials*, 5:735, 2006.

[15] R. Giridharagopal, G. E. Rayermann, G. Shao, G. T. Moore, O. G. Reid, A. F. Tillack, D. J. Masiello, and D. S. Ginger. Submicrosecond time resolution atomic force microscopy for probing nanoscale dynamics. *Nano Letters*, 12:893–898, 2012.

[16] Z. Schumacher, A. Spielhofer, Y. Miyahara, and P. Grutter. The limit of time resolution in frequency modulation atomic force microscopy by a pump-probe approach. *Applied Physics Letters*, 110(5):053111, jan 2017.

[17] S. Yoshida, Y. Terada, M. Yokota, O. Takeuchi, H. Oigawa, and H. Shigekawa. Optical pump-probe scanning tunneling microscopy for probing ultrafast dynamics on the nanoscale. *The European Physical Journal Special Topics*, 222:1161–1175, 2013.

[18] S. Yoshida, Y. Terada, R. Oshima, O. Takeuchi, and H. Shigekawa. Nanoscale probing of transient carrier dynamics modulated in a gaas-pin junction by laser-combined scanning tunneling microscopy. *Nanoscale*, 4:757, 2012.

[19] Y. Terada, S. Yoshida, O. Takeuchi, and H. Shigekawa. Real-space imaging of transient carrier dynamics by nanoscale pump-probe microscopy. *Nature Photonics*, 4:869–874, 2010.

[20] Y. Terada, S. Yoshida, O. Takeuchi, and H. Shigekawa. Laser-combined scanning tunnelling microscopy for probing ultrafast transient dynamics. *Journal of Physics: Condensed Matter*, 22:264008, 2010.

[21] T. L. Cocker, V. Jelic, M. Gupta, S. J. Molesky, J. A. J. Burgess, G. Reyes, L. V. Titova, Y. Tsui, M. R. Freeman, and F. A. Hegmann. An ultrafast terahertz scanning tunnelling microscope. *Nature Photonics*, 7(8):620–625, jul 2013.

[22] S. Yoshida, Y. Aizawa, Z. H Wang, R. Oshima, Y. Mera, E. Matsuyama, H. Oigawa, O. Takeuchi, and H. Shigekawa. Probing ultrafast spin dynamics with optical pump-probe scanning tunnelling microscopy. *Probing ultrafast spin dynamics with optical pump-probe scanning tunnelling microscopy*, 9:1–6, 2014.

[23] S. Grafstrom. Photoassisted scanning tunneling microscopy. *Journal of Applied Physics*, 91:1717, 2002.

[24] Durmus U. Karatay, Jeffrey S. Harrison, Micah S. Glaz, Rajiv Giridharagopal, and David S. Ginger. Fast time-resolved electrostatic force microscopy: Achieving sub-cycle time resolution. *Review of Scientific Instruments*, 87(5):053702, may 2016.

[25] T. L. Cocker, D. Peller, P. Yu, J. Repp, and R. Huber. Tracking the ultrafast motion of a single molecule by femtosecond orbital imaging. *Nature*, 539(7628):263–267, nov 2016.

[26] M. A. Huber, F. Mooshammer, M. Plankl, L. Viti, F. Sandner, L. Z. Kastner, T. Frank, J. Fabian, M. S. Vitiello, T. L. Cocker, and R. Huber. Femtosecond photo-switching of interface polaritons in black phosphorus heterostructures. *Nature Nanotechnology*, 12(3):207–211, dec 2016.

[27] V. Jelic, K. Iwaszczuk, P.H. Nguyen, Rathje C., G.J. Hornig, H.M. Sharum, J.R. Hoffman, M.R. Freeman, and F.A. Hegmann. Ultrafast terahertz control of extreme tunnel currents through single atoms on a silicon surface. *Nature Physics*, 13:591, 2017.

[28] B. Schuler, S. Liu, Y. Geng, S. Decurtins, G. Meyer, and L. Gross. Contrast formation in Kelvin probe force microscopy of single π-conjugated molecules. *Nano letters*, 14(6):3342–6, jun 2014.

[29] Leo Gross, Fabian Mohn, Nikolaj Moll, Peter Liljeroth, and Gerhard Meyer. The Chemical Structure of a Molecule Resolved by Atomic Force Microscopy. *Science*, 325(5944):1110–1114, aug 2009.

[30] L. S. C. Pingree, O. G. Reid, and D. S. Ginger. Electrical Scanning Probe Microscopy on Active Organic Electronic Devices. *Advanced Materials*, 21(1):19–28, jan 2009.

[31] A. Roy-Gobeil, Y. Miyahara, and P. Grutter. Revealing Energy Level Structure of Individual Quantum Dots by Tunneling Rate Measured by Single-Electron Sensitive Electrostatic Force Spectroscopy. *Nano Letters*, 15(4):2324–2328, apr 2015.

[32] G. Binnig, H. Rohrer, C. Gerber, and E. Weibel. Surface studies by scanning tunneling microscopy. *Physical Review Letters*, 49:57, 1982.

[33] G. Binnig and C. F. Quate. Atomic force microscope. *Physical Review Letters*, 56:930, 1986.

[34] Y. Martin, C. C. Williams, and H. K. Wickramasinghe. Atomic force microscope–force mapping and profiling on a sub 100-Å scale. *Journal of Applied Physics*, 61:4723, 1987.

[35] R. García and R. Pérez. Dynamic atomic force microscopy methods. *Surface Science Reports*, 47:197–301, 2002.

[36] Q. Zhong, D. Imniss, K. Kjoller, and V.B. Elings. Fractured polymer/silica fiber surface studied by tapping mode atomic force microscopy. *Surface Science*, 290:L688, 1993.

[37] H. J. Butt and M. Jaschke. Calculation of thermal noise in atomic force microscopy. *Nanotechnology*, 6:1–7, 1995.

[38] J. E. Sader. Frequency response of cantilever beams immersed in viscous fluids with applications to the atomic force microscope. *Journal of Applied Physics*, 84:64–76, 1998.

[39] R.W. Stark and W. M. Heckl. Fourier transformed atomic force microscopy: tapping mode atomic force microscopy beyond the Hookian approximation. *Surface Science*, 457:219–228, 2000.

[40] B. Gotsmann, C. Seidel, B. Anczykowski, and H. Fuchs. Conservative and dissipative tip-sample interaction forces probed with dynamic AFM. *Physical Review B.*, 60:11051–11061, 1999.

[41] F. J. Giessibl. Forces and frequency shifts in atomic-resolution dynamic-force microscopy. *Physical Review B.*, 56:16010–16015, 1997.

[42] U. Dürig. Relations between interaction force and frequency shift in large-amplitude dynamic force microscopy. *Applied Physics Letters*, 75:433, 1999.

[43] U. Dürig. Interaction sensing in dynamic force microscopy. *New Journal Physics*, 2:5.1–5.12, 2000.

[44] J. Tobik, I. Stich, R. Perez, and K. Terakura. Simulation of tip-surface interactions in atomic force microscopy of an InP(110) surface with a Si tip. *Physical Review B*, 60:11639, 1999.

[45] I. Stich, J. Tobik, R. Perez, K. Terakura, and S.H. Ke. Tip-surface interactions in noncontact atomic force microscopy on reactive surfaces. *Progress in Surface Science*, 64:179–191, 2000.

[46] A.I. Livshits, A.L. Shluger, A.L. Rohl, and A.S. Foster. Model of noncontact scanning force microscopy on ionic surfaces. *Physical Review B*, 559:2436, 1999.

[47] N. Sasaki and M. Tsukada. Theory for the effect of the tip–surface interaction potential on atomic resolution in forced vibration system of noncontact afm. *Applied Surface Science*, 140:339, 1999.

[48] N. Sasaki and M. Tsukada. New method for noncontact atomic force microscopy image simulations. *Japanese Journal of Applied Physics*, 38:192, 1999.

[49] S. Sadewasser and T. Glatzel. *Kelvin Probe Force Microscopy*, chapter 1, pages 3–20. Springer Nature, 2018.

[50] J. N. Israelachvili. *Intermolecular and Surface Forces*. Elsevier LTD, Oxford, 1985.

[51] R. Perez, M. C. Payne, I. Stich, and K. Terakura. Role of covalent tip-surface interactions in noncontact atomic force microscopy on reactive surfaces. *Physical Review Letters*, 78:687, 1997.

[52] L. N. Kantorovich and T. Trevethan. General theory of microscopic dynamical response in surface probe microscopy: From imaging to dissipation. *Physical Review Letters*, 93:236102, 2004.

[53] Z. Schumacher. *Time-domain Kelvin Probe Force Microscopy for Local Ultra-Fast Decay Time Measurements*. PhD thesis, McGill University, Montreal, Quebec, 2016.

[54] TOPTICA Photonics AG, Lochhamer Schlag 19, D-82166 Graefelfing/Munich, Germany. *FemtoFiber pro: Ultrafast Erbium Fiber Laser System*, 6 edition, 6 2015.

[55] D. J. J. Hu, R. T. Murray, T. Legg, T. H. Runcorn, M. Zhang, R. I. Woodward, J. L. Lim, Y. Wang, F. Luan, B. Gu, P. P. Shum, E. J. R. Kelleher, S. V. Popov, and J. R. Taylor. Fiber-integrated 780 nm source for visible parametric generation. *Optics Express*, 22(24):29726–29732, Dec 2014.

[56] E. P. Ippen and C. V. Shank. *Techniques for Measurement*, chapter 3, pages 266–290. Springer-Verlag, 1984.

[57] H. P. Weber. Method for pulsewidth measurement of ultrashort light pulses generated by phase-locked lasers using nonlinear optics. *Journal of Applied Physics*, 38:2231, 1967.

[58] J. A. Armstrong. Measurement of picosecond laser pulse widths. *Applied Physics Letters*, 10:16–18, 1967.

[59] J. C. Diels, W. Rudolph, Liao P., and P. Kelley. *Ultrashort Laser Pulse Phenomena: Fundamentals, Techniques, and Applications on a Femtosecond Time Scale*. Academic Press, Burlington, MA, 1 edition, 1996.

[60] M. Maier, W. Kaiser, and J. A. Giordmaine. Intense light bursts in the stimulated raman effect. *Physical Review Letters*, 17:1275–1277, 1966.

[61] F. X. Kaertner. Ultrafast optics. Lecture Notes, 2005. Massachusetts Institute of Technology.

[62] A. Owyoung. *The Origins of the Nonlinear Refractive Indices of Liquids and Glasses*. PhD thesis, California Institute of Technology, California, United States, 1971.

[63] R. W. Boyd. *The Nonlinear Optical Susceptibility*, chapter 1, pages 1–67. Academic Press, 2008.

[64] E. Goulielmakis, V. S. Yakovlev, A. L. Cavalieri, M. Uiberacker, V. Pervak, A. Apolonski, R. Kienberger, U. Kleineberg, and F. Krausz. Attosecond control and measurement: Lightwave electronics. *Science*, 317(5839):769–775, 2007.

[65] J. A. Armstrong, N. Bloembergen, J. Ducuing, and P. S. Pershan. Interactions between light waves in a nonlinear dielectric. *Phys. Rev.*, 127:1918–1939, Sep 1962.

[66] M. M. Fejer, G. A. Magel, D. H. Jundt, and R. L. Byer. Quasi-phase-matched second harmonic generation: tuning and tolerances. *IEEE Journal of Quantum Electronics*, 28:2631 – 2654, 1992.

[67] O. A. Castañeda-Uribe, R. Reifenberger, A. Raman, and A. Avila. Depth-sensitive subsurface imaging of polymer nanocomposites using second harmonic kelvin probe force microscopy. *ACS Nano*, 9:2938–2947, 2015.

[68] J. Dai and X.C. Zhanga. Terahertz wave generation from gas plasma using a phase compensator with attosecond phase-control accuracy. *Applied Physics Letters*, 94:021117, 2009.

[69] A. Dhar and A. Mansingh. Optical properties of reduced lithium niobate single crystals. *Journal of Applied Physics*, 68(11):5804–5809, 1990.

[70] S. A. Burke, J. M. LeDue, Y. Miyahara, J. M. Topple, S. Fostner, and P. Grutter. Determination of the local contact potential difference of ptcda on nacl: a comparison of techniques. *Nanotechnology*, 20:264012, 2009.